Rochester Institute of Technology

RIT Digital Institutional Repository

Spring 2019

Atomistic Simulation for Transition Metal Dichalcogenides using NEMO5 and MedeA-VASP

Udita Kapoor
uk8532@rit.edu

Follow this and additional works at: https://repository.rit.edu/theses

Atomistic Simulation for Transition Metal Dichalcogenides using NEMO5 and MedeA-VASP

Udita Kapoor

Atomistic Simulation for Transition Metal Dichalcogenides using NEMO5 and MedeA-VASP

UDITA KAPOOR

Spring 2019

A Thesis Submitted
in Partial Fulfillment
of the Requirements for the Degree of
Master of Science
in
Microelectronic Engineering

R·I·T | KATE GLEASON
College of ENGINEERING

Department of Electrical and Microelectronic Engineering

Atomistic Simulation for Transition Metal Dichalcogenides using NEMO5 and MedeA-VASP

Udita Kapoor

Committee Approval:

Dr. Sean Rommel *Advisor*   Date
Gleason Professor of Electrical and Microelectronic Engineering

---

Dr. Karl Hirschman   Date
Professor, Microelectronic Engineering

Dr. Santosh Kurinec   Date
Professor, Microelectronic Engineering

Dr. Robert Pearson   Date
Program Director, Microelectronic Engineering

Dr. James E. Moon   Date
Professor, Electrical and Microelectronic Engineering

Dr. Jing Zhang   Date
Professor, Electrical and Microelectronic Engineering

Dr. Sohail A. Dianat   Date
Department Head of Electrical and Microelectronic Engineering

Acknowledgments

This thesis marks the culmination of my master's in microelectronics. This journey included stories of a lot of people without whom this wouldn't have come to my reality. First and foremost my father, mother and my sister who inculcated my curious eyed point of view and I am really grateful to them for everything that they are and for everything they made me. I would like to dearly thank Dr. Sean Rommel for introducing me to this world of atomistic simulations and always being there for me in times of doubts, questions, laughter, so patiently. Thank you for being so brilliant at things that you do and always keeping the environment encouraging. I would like to thank Dr. Kurinec and Dr. Moon for their wonderful insights on the topic and especially for teaching me microelectronics and device physics so well that I was able to question and understand the working of complex models and devices. They have built the foundations without which none of this would have been possible. I am thankful to Dr. Pearson for being so understanding and patient all this time. He has seen us come as lost master's kids, new to both the subject and the place, and he made this journey as comfortable and challenging as he could. And my very dear partner in this endeavor, Patsy Cadareanu, who recently presented her work on quantum simulations of III-V Esaki diodes and 2D semiconductors. She is a joy to be around with and a very humble and fun person to work with. Patsy, Dobby, and Egg have made this time very calm and entertaining. Her thesis has been a reference point for me. The support team for NEMO, Jim Fonseca, Dr. Tillman, Gerhard Klimeck from Purdue University and the Material design support team including but not limiting to, Ray Shan and Volker Eyert have been very helpful in building our understanding of NEMO and MedeA-VASP for which both my advisor and I are grateful. And Wolfy, thank you.

To my family ...

Abstract

This thesis is an attempt to understand and delve into the realm of atomistic simulations, using it to understand a novel set of materials called Transition Metal Dichalcogenides (TMDs). We use NEMO5 and MedeA-VASP to calibrate and characterize a few selected TMDs and to validate our understanding of atomistic modeling we simulated a tunnel field-effect transistor with monolayer TMD as a channel using NEMO5. TFETs offer great advantages over MOSFET (metal oxide field effect devices) like, sub-60 mV/dec sub-threshold swing, minimal leakage current, high switching speed, and small power requirements. Low drive current has prevented TFETs from becoming a mainstream device instead of MOSFETs. Two methods of improving TFETs are being considered: one, making the device out of single-layered materials, and two, using different kinds of materials, TMDs being one of them. This research uses NEMO5 and MedeA-VASP atomistic modeling tools to understand both of the device improvement approaches mentioned above. Variation in parameters that matter at the atomic scale, like high symmetry k-point path, k-point meshing, and plane-wave cut-off energy exhibit prominent effects on the band-structure of a material. NEMO5 E-k band structures were simulated for TMDs like MoS_2 and WTe_2 and the band-gap structures obtained were compared with literature. Structure definition and atomistic device simulation were conducted in NEMO5. A TFET with a monolayer of MoS_2 as a channel was simulated to see the I-V characteristics obtained from the NEMO5 tool. By performing electronic band-structure simulations with and without spin-orbit coupling (SOC) and comparing it against electronic structures presented in literature, it is shown that consideration of SOC is necessary for accurate results. Atomistic simulations are computationally intensive and this work also explored the effects of parametric and distributed computing settings on simulation times.

Contents

List of Figures

List of Tables

List of Symbols

Term	Description	Units/Value
C'_D	Depletion region capacitance per unit area	F/cm^2
C'_{ox}	Oxide capacitance per unit area	F/cm^2
$\mathcal{E}$	Electric field	V/cm
E_c	Energy at the conduction band edge	eV
E_F	Fermi level	eV
E_g	Band gap energy	eV
E_v	Energy at the valence band edge	eV
E_x, E_y	Electric field normal and parallel to the gate	V/cm
$\hbar$	Reduced Planck constant	6.582×10^{-16} eV·s
I_D	Drain current	A
J_t	Band to band tunneling current density	A/cm^2
k	Boltzmann's constant	8.617×10^{-5} eV/K
m^*	Carrier effective mass	kg
N_A	Acceptor concentration	cm^{-3}
N_c	Effective density of states in the conduction band	cm^{-3}
n_i	Intrinsic carrier concentration	cm^{-3}
q	Elementary charge	1.602×10^{-19} C
S	Subthreshold swing	V/dec
T	Temperature	K
V_{DS}	Drain–Source voltage	V
V_{eff}	Effective reverse bias voltage	V
V_{FB}	Flatband voltage	V
V_G	Gate voltage	V
ϵ_s	Permittivity of a semiconductor	F/cm
μ_n, μ_p	Mobility of electrons and holes, respectively	cm/V·s
Ψ_s	Surface potential	V

List of Acronyms

Term	Description
TMD	Transition Metal Dichalcogenide
SOC	Spin Orbit Coupling
DOS	Density of States
DTF	Density Functional Theory
NEGF	Non Equilibrium Green's Functional
QTBM	Quantum Transmitting Boundary Method
VASP	Viena ab-initio Simulation Package
SCF	Self Consistent Function
GGA	Generalized Gradient Approximation
LDA	Local Density Approximation
TFET	Tunneling Field Effect Devices
BZ	Brillouin Zone
ATK	Atomistic Took Kit
TCAD	Technology Computer Aided Design
WKB approximation	Wentzel Kramers Brillouin approximation

Chapter 1

<div align="right">

Introduction and Motivation

</div>

In order to improve our knowledge of materials and devices, it is common to start with a theoretical model. Subsequently the model is validated for the robustness of those equations for other materials and devices, alter variables to customize the model parameters and once some understanding of the electrical behavior is acquired, start optimization of the model parameters. ITRS (International Technology Roadmap for Semiconductors)[21] has been used as a standard benchmark for measuring evolution in this industry and it has predicted a probable bottleneck in the growth of the semiconductor industry once device scaling reaches a physical limit. FinFETs have been able to solve for the lateral scaling needs of the device so far and show promising results for scaling down to 7nm devices. But beyond 7nm, devices have shown additional thermal side effects, higher power dissipation, heat accumulation at the fingers and self-heating [22]. With this work, we intend to focus on the scaling aspect by using monolayers to increase gate control. In order to simulate a device with the thickness of the order of single unit cell, we needed simulation tools and numerical models that solve for electronic behavior at the atomistic level. This work was inspired by multiple research groups who have invested heavily in atomistic simulation projects.

The center for Low Energy System's Technology (LEAST) is a research group that is currently funding 12 universities and working in collaboration with 6 major com-

panies, including but not limited to Micron, Texas Instrument, IBM, and Raytheon. IBM and D-wave have already established a market for commercial quantum computers and made themselves primary suppliers of those systems. Very recently, Silvaco (whose TCAD tools we use at our University to train students in process simulations) acquired the nano-electronics modeling software NEMO5 that came out of a research group from Purdue headed by Dr. Gerhard Klimeck. This thesis is extensively focused on the working and operation of NEMO5 tool used for atomic level quantum simulation. Looking around, from powerful establishments like Google and Tesla to startups budding in the semiconductor industry, all are aiming for smaller and better devices. These activities establish the financial and innovative interest in atomistic simulations. The need for low power, low leakage, smaller footprint, high current drive, and a steep sub-threshold slope is evident. The purpose of initiating research based on atomistic simulation at RIT is to have an understanding of TFET devices, to enable atomistic simulations and to optimize them. The aim is to enter in the professional world as better equipped engineers. The purpose of this study is to characterize novel TMD materials using atomistic simulators (NEMO5 and VASP) and further to simulate the operation of a monolayer TMD in a tunneling field-effect device. High leakage current in small devices have called for the development of tunneling devices. Through this study, we aimed at understanding the atomistic simulation that can be used to optimally emulate high-end tunneling and quantum devices. Dr. Salahuddin [23] in his very recent publication introduces this phase of scaling devices as hyper-scaling.

This project also intends to increase the footprint of simulation and design-based research in RIT's Microelectronic department. Primarily for this thesis, we used an outsourced server space from Purdue University, which hosts NEMO5, wherein a reasonable amount of time was consumed in queuing of jobs. Owning to large computational needs of heavy duty programs like NEMO5 and VASP, we acquired a

new 36 core processor with high-end GPU that allowed us to cut down our run time by a reasonable margin. But now, with our own systems in place, quick screen tests can be performed before submitting the jobs to higher power servers for complex and many point calculations.

1.1   Need for Atomistic Simulations

The main motivation for simulations is optimized process and device design. Processes and devices have been modeled so far in a classical manner using TCAD modeling methods. These methods have been tested and benchmarked against experimental data for macro and micro-devices and having sustained years of experimentation, TCAD modeling has been established as an economical and reliable tool for modeling semiconductor devices for a wide range of materials. But the persistent scaling down of devices has reached a point where the physical dimensions of the active device have come down to a countable number of atoms [24]. The charge transport at the atomistic level reaches the ballistic regime. Nano-electronic phenomena like tunneling, scattering, atomistic disorder, and phonon emission have become dominant in such devices and the numerical models used so far for TCAD modeling have proven to be insufficient in modeling them accurately. This calls for the need of numerical models that operate at the atomistic level. The moment scales reach atomistic levels, the output obtained are in terms of probabilities instead of discrete values. A nano-electronic atomistic solver like NEMO5 consists of numerical models that operate on solving the Poisson equation and the Schrodinger equation self consistently starting from an initial guess. The reproducibility of such calculations can prove to be reliable only when the system is very accurately calibrated, which needs multiple iterations and experiments. This study is therefore a call for more such experiments so that the simulation tools can be appropriately calibrated and be efficiently used to explore the unknown technology and materials.

TFET device operation at the atomic scale has the benefits of small footprint, high switching speed, and low power consumption. But it also faces issues like high leakage current and small drive current. The main parameters characterizing the operation of diffusion transport device are sub-threshold swing (SS) and the I_{ON}/I_{OFF} ratio. Sub-threshold swing is the value of gate voltage required to change the drain current by a factor of 10 and is given by equation 1.1:

$$SS(real) = \frac{\kappa T n}{q} ln(10) \qquad (1.1)$$

where n is a dimensionless quantity that factors in the non-ideal behavior and T is the temperature. This shows that at room temperature one can have a minimum of 60 mV/dec SS. The only way to surpass this limit is to move from diffusive transport to tunneling transport, leading to the requirement of tunneling devices like Esaki diodes and tunneling field-effect devices (TFETs).

Transition metal dichalcogenides (TMDs) belong to a group of materials that consists of transition metals like tungsten and molybdenum with chalcogens like sulfur and selenium. The research in using TMD materials as possible material for electronic devices is only about a decade old, therefore studying them was interesting and challenging. TMDs have an electronic configuration where d-orbitals are partially filled and are non-bonding which sets them apart from other molecular systems. The non-bonding d-orbital gives rise to van der-Waal forces between two consecutive layers which makes exfoliation of mono-layers from bulk materials easy. These unique properties of TMD materials allows them to have tunable bandgap, surface free of dangling-bonds, and easy extraction of thin layers for prototyping a device.

1.2 Current state of research in TMD devices

With a certain section of research in semiconductors focused specifically on the scaling of devices, a relentless search in finding 2-D semiconducting devices is going on. Along with graphene layers and black phosphorus, TMDs have also been rigorously researched. TMDs particularly stand out because of their strong in-plane bonds, therefore, preventing any atomic diffusion into other layers like the substrate and so provides a strong thickness control [25]. They have the ability to establish van der-Waal bonds with other 2-D layers giving way to tunable band-gaps, an ability to form hetero/homo-junctions and no dangling bonds. About 126 transition metal dichalcogenides have been studied so far, but a small percentage of them have made it to experimental studies[26]. A few compounds have been found to be unstable in air and the rest are under consideration [26]. Tungsten and molybdenum are the most studied elements, combined with chalcogens like sulfur, selenium, and tellurium.
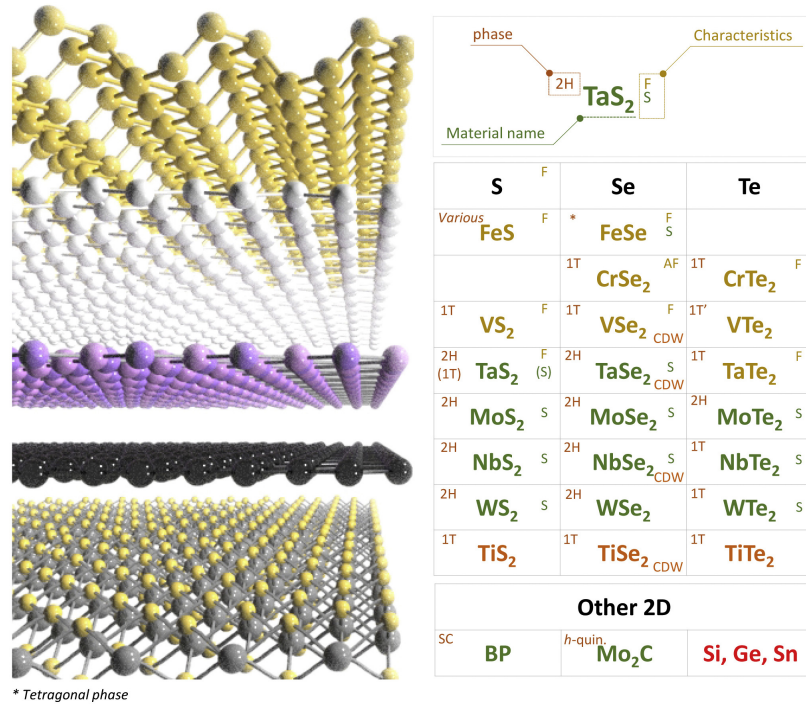
Figure 1.1: A short list of various TMD materials in research[1]

Figure 1.1 shows an example chart of different kinds of TMDs under research. So far there has been not enough experimental data gathered to have a consensus on the band gap of these materials. Molybdenum disulfide and tungsten ditelluride, as Aron *et. al* very clearly mentions in his study of *Ab initio* simulations for 2-D materials [27], even after being rigorously studied so far, have not reached a consensus in terms of lattice constants and band gap. This thesis refers to his study as well for band gap and simulation information. Study shows, by the year 2015, about 5000 research publications were published on 2D material [1] and market research shows that atomistic computation market will grow over $2 billion by the year 2020 [28] (Figure 1.2). With the trends shown in Figure 1.2, it is evident that the scope of atomistic modeling is growing at an exponential rate thus calling for the need for more people equipped with the understanding of both the device physics at the atomic scale as well as simulation of systems that can be used to make devices at the atomic scale. This simulation-based study, therefore, becomes one of the stepping stones for the future research.

There have been many studies that have discussed the electronic structure of TMDs. Table 1.1 is a small collection of different simulation setups used by some of the researchers, specifically for molybdenum disulfide and tungsten ditelluride. The table consists of three parameters that have been shown to greatly affect the simulation of the electronic properties a lot: k-space matrix, "a" lattice constant of the unit cell and the numerical models used for obtaining the band-structure.

Material	k-space matrix	"a" lattice	Model Used	E_g (D/I)	Ref
MoS_2	12x12x1	0.319 nm	(VASP) GGA-PBE	1.59 eV (D)	[29]
MoS_2	25x25x1	-	(VASP) GGA-PBE	1.67 eV	[27]
MoS_2	20x4x1	-	(ATK) GGA-PBE	1.805 ev (D)	[5]
MoS_2	31x31x1	0.3122 nm	(EXC!TING) PBE	1.79 eV (D)	[19]
WTe_2	40x40x1	0.356 nm	(VASP)GGA-PBE	0.74 eV(D)	[29]
WTe_2	-	-	*ab initio*	0.75 eV (D)	[30]

Table 1.1: Experimental setup from various literature on TMD material characteristics(not extensive)

(a) Budget predicted for atomistic computing[28]
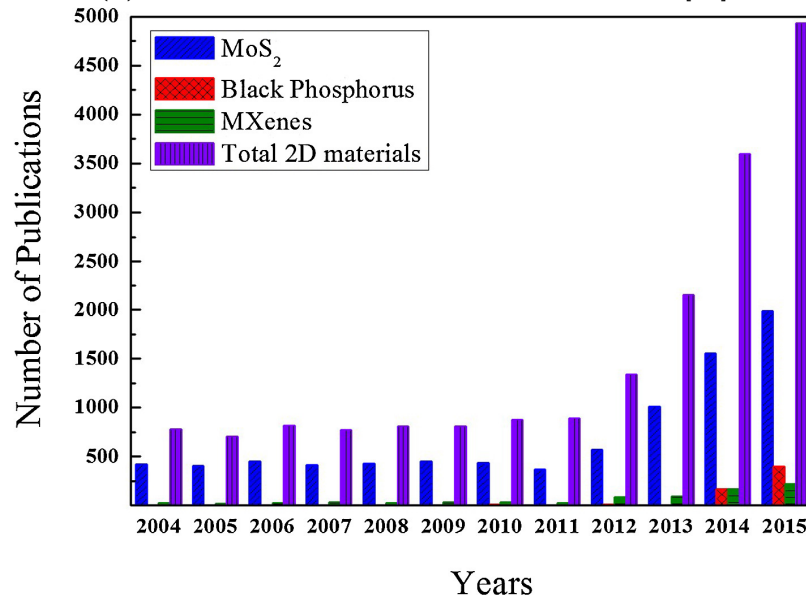
(b) Literature survey of 2-D material[1]

Figure 1.2: Literature survey of research in 2-D material as of 2015 and the predicted market for quantum computing by 2020

In Table 1.1 k-space matrix or k-points can be defined as the number of points in the k-space of the material's Brillouin zone along which the band structure is calculated. The importance of this parameter lies in the determining the accuracy of the bandstructure and in estimation of the computational time. The other parameter mentioned in Table 1.1 is lattice constant "a" and "c". They correspond to the dimensions of the unit cell in x-direction and z-direction respectively (where z-direction

is the height). The value of these lattice parameters is of prime importance in calculating the bandgap of a material as they decide the electrostatic interaction between the atoms of the material. The "c" parameter in particular controls the distance between two consecutive monolayers layers of material. Therefore, in order to simulate the band-structure and electronic behavior of a monolayer, the system should be set up in a such a way that "c" is large enough to eliminate any electrostatic interaction between the two layers of the material.

It is evident from Table 1.1 that with the same model used for band-structure calculations for MoS_2, two studies show two different values for band-gap: according to one, a monolayer of MoS_2 should have an E_g of 1.59 eV, and according to another, a monolayer of MoS_2 should have an E_g of 1.805 eV. There clearly seems to be a lack of consensus. Therefore, in this work, we investigate these parameters and compare the results obtained with additional publications. We also initiate the call for conducting more atomistic simulation-based projects.

1.3 Thesis Outline

This thesis is primarily divided into three sections: Chapter 1 introduces the need for simulation-based research, and serves to enlighten potential researchers. Chapter 2, Chapter 3 and Chapter 4 deal with the theory of devices, atomistic modeling and transition metal dichalcogenide materials. Chapters 2 and 4 are foundations needed for the final chapters, 5 and 6 dealing with results and discussion for the simulations conducted in this project. Chapter 5 discusses only the material characterization of the TMD materials. This section segues into Chapter 6 which is a discussion about simulated tunnel diodes and a tunnel field-effect device consisting of III-Vs and a monolayer channel of MoS_2, respectively. Chapter 7 summarizes the project and provides with the final conclusions. It also briefly discusses the future prospects of this research.

Chapter 2

Theory of Transition Metal Dichalcogenides: Novel Materials

2.1 Introduction

Transition metal dichalcogenides (TMDs) are known to date back to about 2.9 billion years [3], yet studying TMDs as probable device material is only about a decade old. There are over 88 TMDs known in bulk form [26] out of which a considerable number could be exfoliated into 2D layers. Filip *et al.* presented an extensive study of 51 TMD materials, comparing the band-structures and electronic properties via simulations using local density approximation [26].

TMDs fall under the category of layered materials like graphene, which is graphite in monolayer form. They are known to cover a wide range of electrical properties: from insulating, to semiconducting, to metallic. With a general molecular formula MX_2, transition metal dichalcogenides consist of chalcogens (Group VI, e.g., S, Se,Te) elements (X) sandwiching a transition metal (Group IV, e.g., Mo, W) (M). These elements' position in the periodic table can be seen in Figure 2.1.

The molecule is sp^3 hybridized with a non-bonding d-orbital in a plane perpendicular to other orbitals. This leads to weak van-der Waal forces between two layers. The system consists of 6 anti-bonding orbitals which are partially occupied and therefore it provides high mobility to the occupying electrons [3]. Due to this sp^3 hybridization the electronic properties of TMD materials range from metallic, NbS_2 to insulating,

Figure 2.1: Periodic table highlighting transition metal dichalcogenides [2]

HfS_2. The more interesting ones lie in the semiconducting range, like MoS_2, $MoSe_2$, WS_2, to name a few.
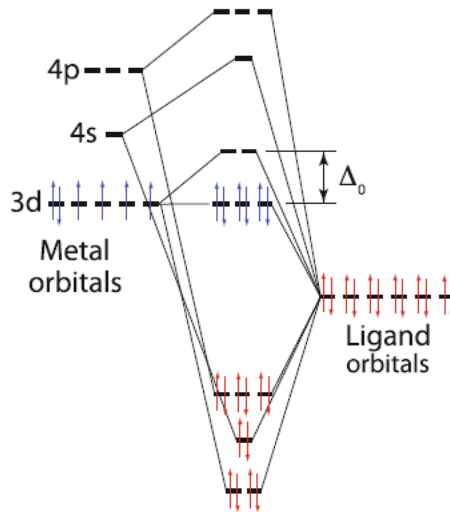
Figure 2.2: Molecular orbital configuration of transition metals according to ligand-field theory [3].

Figure 2.2 shows the electronic configuration of $Co(NH_3)_6^{-3}$, another TMD ion. It is presented here to give a basic understanding of the electronic configuration of TMD molecules. The electronic properties in TMDs are not only guided by the electronic configuration of the system, but also by the stacking of molecular layers. Figure 2.3 shows a bilayer configuration of WTe_2 with hybridized orbitals shown in pink.
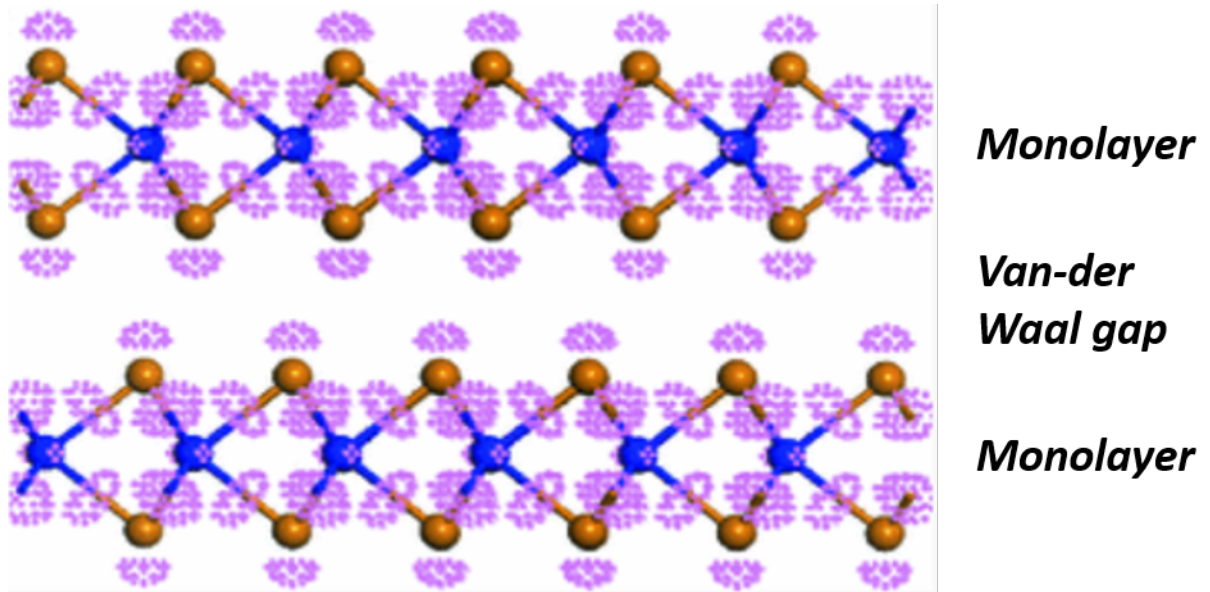
Figure 2.3: DFT relaxed structure of $MoTe_2$ with charge density clusters (pink, cloud like) demonstrating charge accumulation in the van-der Waal gap associated with sp^3 hybridization of chalcogen atoms [3].

The figure shows the presence of non-reactive lone-pair electrons in d-orbital of the chalcogen (the pink lobes between the two layers). These electrons do not participate in chemical bonding which prevents the two layers of $MoTe_2$ from getting linked to each other. They instead stay attracted towards each other only via weak van der Waal's forces. This is the case with TMDs; the materials that have an inert pair of lone-pair electrons in their valence orbital.

The text by Alexander V. Kolobov and Junji Tominaga [3] provides many additional details of importance in various other transition metal dichalcogenides and their structural characteristics. In order to progress with actual simulations, this work will focus on a smaller subset of the possible materials. Following sections briefly discuss a few well-known TMD materials, namely molybdenum disulfide, tungsten ditelluride, and tungsten disulfide. The sections discuss the crystal properties and the band-structure for bulk, bi-layer and monolayer systems of the mentioned materials.

2.2   Molybdenum Disulfide (MoS2)

2.2.1   Crystal Structure

Molybdenum disulfide (MoS_2) is one of the most researched TMD materials. It is a
layered transition metal dichalcogenide with an indirect band-gap of 1.23 eV in bulk
configuration. There exist two stable structural polytypes of MoS_2. One is trigonal
prismatic (2H) which is semiconducting in nature and the other is octahedral symme-
try which is known to be metallic [31]; both are shown in Figure 2.4. In 2-H configu-
ration each molybdenum atom is sandwiched between two sulfur atoms via covalent
bonds forming a hexagonal structure and multiple layers are stacked against each
other via van der Waal's forces thereby making the process of obtaining monolayer
easy. The surface of bulk molybdenum disulfide along the (0001) plane is chemically
inert due to a dearth of any dangling bonds [32], although a particular study cited
in [32] shows chemical reactivity at the edges of single-layer MoS_2 nanocrystallites.
The edges, once strategically reconstructed showed an affinity towards reaction with
cobalt, nickel, and iron, which could be used as potential dopants. The surface de-
fects, bond strain and changing topography can be induced to change the electronic
behavior, but in its natural form, the surface of MoS_2 lack defects.

Molybdenite in mineral form, MoS_2 has crystal lattice constants equal to 0.316
nm for "a" which is equal to lattice constant "b" and 1.229 nm for lattice constant
"c". The molecule is bound by bond lengths of 0.238 nm between Mo-S and 0.312
nm between S-S atoms [19]. The crystal belongs to space group $p6_3/mmc$ in bulk
configuration and $p6_2/mm$ in monolayer configuration. The hexagonal Bravais lattice
translates to a hexagonal Brillouin zone, as shown in figure 2.5.

The high symmetry points in Figure 2.5 are Γ-M-K when considered for a mono-
layer system and A-L-H that lie directly above and are taken into consideration when
a bulk system is considered.
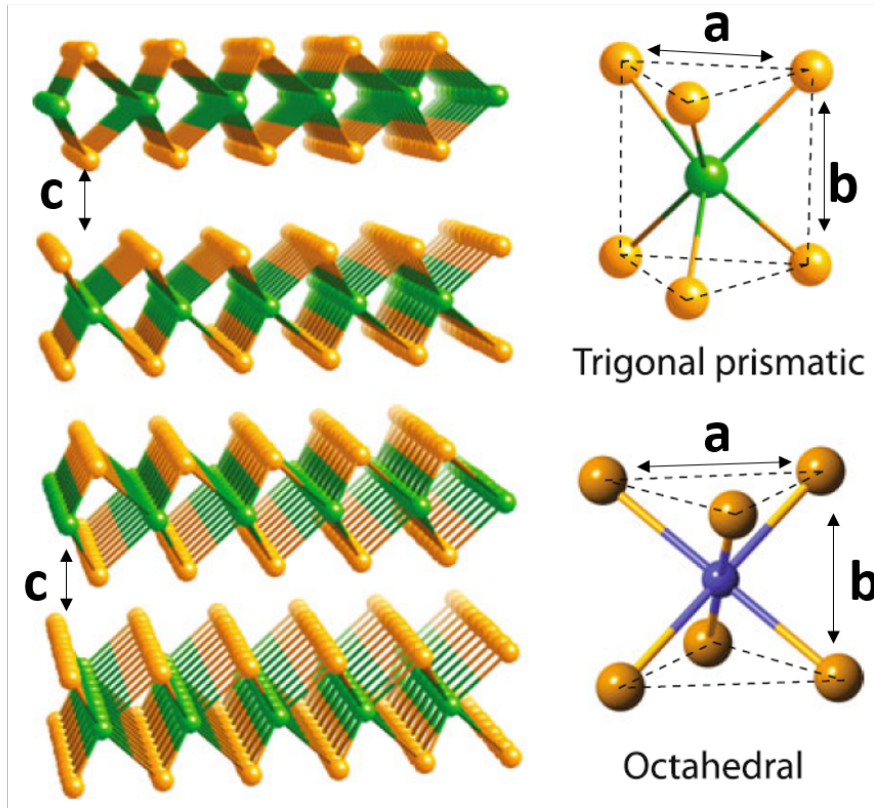
Figure 2.4: Typical MX_2 bulk structure in 2 polytypes: triagonal prismatic and octahedral [3]
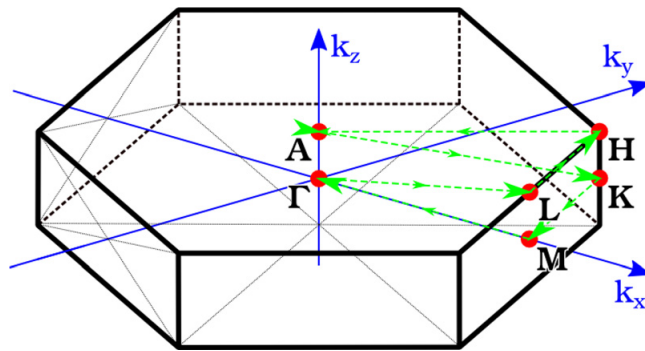
Figure 2.5: Hexagonal Brillouin zone for MoS_2 with high symmetry points [4]

Using the linear combination of atomic orbital theory (LCAO), molecular orbitals' coupling for sp^3d^5 hybridization of MoS_2 was analyzed. The valence orbital for molybdenum, 4d is coupled with the valance orbital for sulfur, 3p in sp^3d^5 hybridization leading to pairing of unpaired d-orbital electrons thereby making the system unreactive and providing more "room" for charge movement (valence orbitals for TMDs

have larger radii in comparison to other elements), leading to high charge mobility.
Due to the fact that in two-dimensional structures the molecular interaction along
the z-axis (height) is negligible, there is limited mobility in the z-direction. This
anisotropic mobility is a known property of other 2D materials as well and is taken
advantage of in designing device channels along the high mobility axis. Even though
2D MoS_2 has the benefit of high charge mobility, there is a dearth of charge carriers
and the system has a small density of states at the high symmetry points. There-
fore, the current drive through devices that consists of MoS_2 monolayer channels is
not known to be very high, unlike a semi-metallic TMD like WTe_2, Figure 2.6. The
concept of increasing charge concentration by introducing surface defects like strain,
charged vacancies etc., is therefore considered a promising area of research for TMDs.

2.2.2 Band Structure

The effect of layering in MoS_2 is observed when its band structure is analyzed. On
transitioning from bulk to monolayer, the system transitions from an indirect band-
gap between Γ-K (with value 1.232 eV) to a direct band-gap at K-K high symmetry
k-points (with value 1.8 eV). Gao *et al.* in his work [5] presented simulated results
showing this transition as shown in Figure 2.7. Eugene *et al* reaffirms this transition
and further points out how the lack of inversion symmetry in a 2D MoS_2 leads to
band-splitting due to spin. This concept is not dealt with in detail in this work but
is of great importance for understanding the optical effects and valley effects in MoS_2
[19].
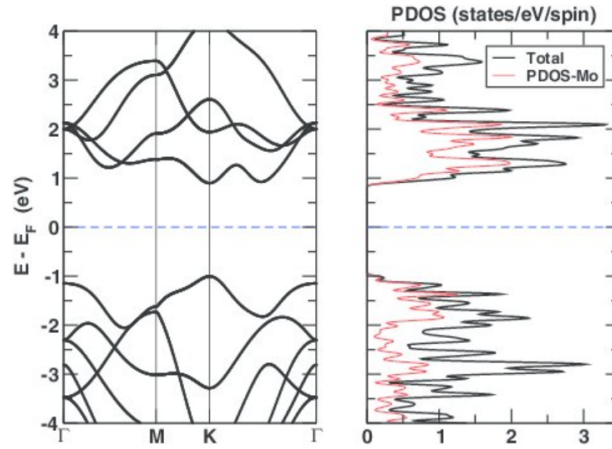
(a) Density of states in monolayer MoS_2 [33]
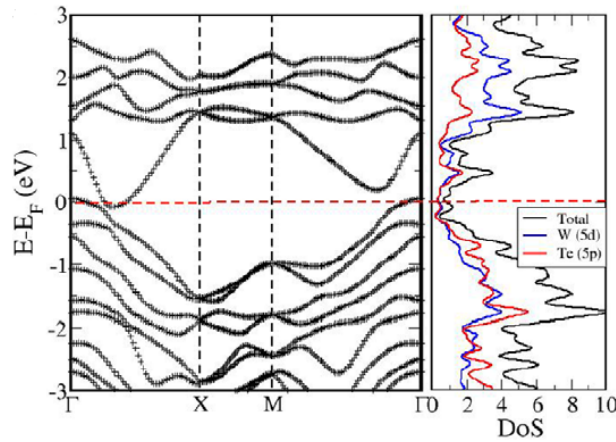
(b) Density of states for monolayer Td-WTe_2 [6]

Figure 2.6: Comparison of DOS for monolayer WTe_2 and MoS_2; WTe_2 DOS is 8 times higher than MoS_2

2.3 Tungsten Di-telluride (WTe2)

2.3.1 Crystal Structure

Tungsten di-telluride, another layered transition metal dichalcogenide, comes under the category of Weyl semi-metals which is a group of solid state crystals with Weyl fermions as their low energy excitation charge carriers. These fermions carry an electric charge even at room temperature leading to easy mobility of charge carriers [6]. Furthermore, the mobility of Weyl fermions is independent of crystal symmetries
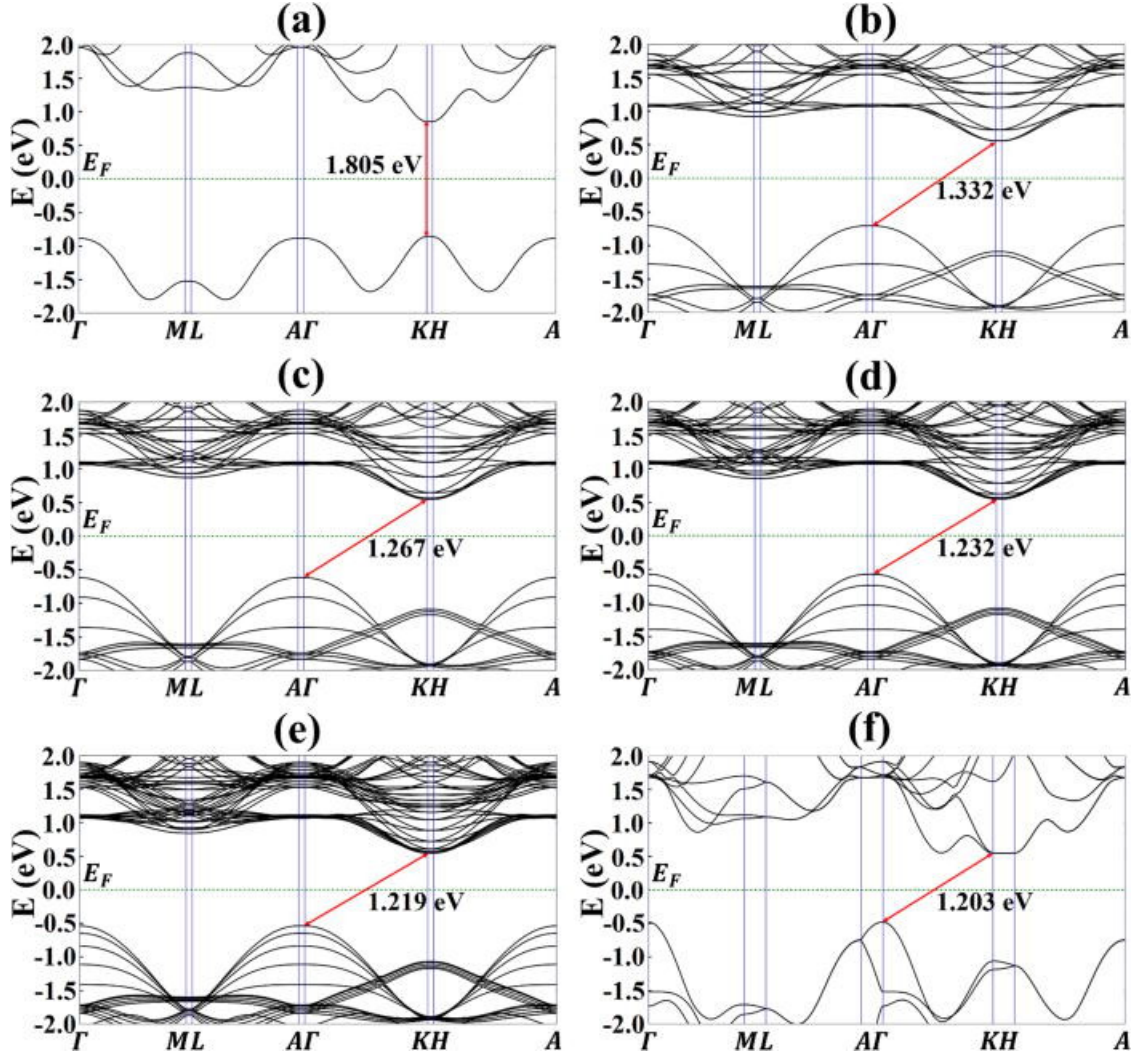
Figure 2.7: MoS$_2$ band-structure from monolayer to bulk system simulated using DFT-metaGGA [5]: (a) bandstructure of monolayer MoS$_2$ with direct bandgap of 1.805 eV present at K k-point in the first BZ. (b) Bandstructure of bilayer MoS$_2$ with an indirect bandgap of 1.332 eV located between Γ point in valence band and K point in conduction band (c)-(e) Bandstructure of 3-5 layers of MoS$_2$ with indirect bandgaps located between Γ point in valence band and K point in conduction band. (f) Bandstructure of bulk MoS$_2$ with indirect bandgap reduced to 1.203 eV located between Γ point in valence band and K point in conduction band

except translational symmetry leading to the high mobility of electric charge in Weyl semi-metals. These metallic properties are observed in the bulk structure of WTe$_2$.

Crystal structure of WTe$_2$ resembles that of molybdenum disulfide but is distorted along "a-axis", i.e. tungsten (W) chain axis. Generally, TMDs exist in either 1T or 2H crystal configuration. Unlike other TMDs, WTe$_2$ is found to be most stable

in distorted 1T configuration (Td) where the distortion is caused by displacement of tungsten atom from the center of telluride octahedral, where one metal atom is surrounded by six chalcogens(tellurium) and two metal atoms (tungsten), as shown in Figure 2.8 [6]. The reason for this distortion is still unclear and under research, although it has been confirmed via Raman spectroscopy that Td-WTe$_2$ has the lowest energy among all the polytypes of WTe$_2$ and therefore is the most stable configuration for it. WTe$_2$ has orthorhombic lattice structure (Brillouin zone) [7] and Pmn21(C^7_{2v}) space group.
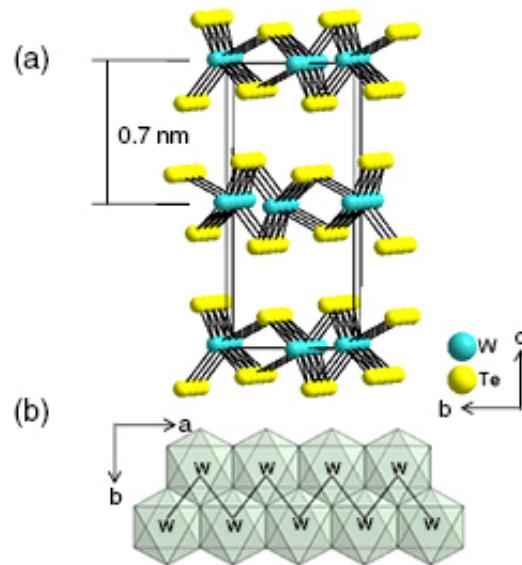
Figure 2.8: (a)Structure of orthorhombic symmetry seen in stacked Td-WTe$_2$ (b)Polyhedral representation of Td-WTe$_2$ showing W atoms' displacement leading to buckling of W chain along "a" axis [6]

WTe$_2$ crystal also shows large non-saturating magneto-resistance and unique thermoelectric properties, making itself stand out among other TMD materials. An interesting review on WTe$_2$ is provided by Tian *et. al* [7].

2.3.2   Band Structure

Tungsten ditelluride belonging to the category of layered TMDs, as discussed above, has a crystal structure which is stacked along c-axis via van der Waal forces. This property, as for other TMDs, can be utilized for tuning electronic gap for the material. The band structure for WTe_2 can be seen in Figure 2.9b, for bulk and monolayer as presented in [6]. Experiments have shown WTe_2 transitions from metallic characteristics to insulating characteristics when reduced from bulk structure to a few layers [7], shown in Figure 2.9a but not enough literature has been found to validate this information. Figure 2.9a shows Y1 axis with conductivity ($\approx e^2/h$) for each layer and Y2 with the corresponding resistivity (ρ) plotted against Temperature (K) on x-axis.

2.4   Tungsten di-sulfide (WS_2)

2.4.1   Crystal Structure

Tungsten disulfide in bulk form has a trigonal prismatic crystal structure resembling that of MoS_2, with a hexagonal Brillouin zone as shown in Figure 2.10. The material belongs to space group $P6_3/mmc$, where a unit cell has a threefold rotational axis about the c-axis and a mirror plane about the position of tungsten atoms. The system, similar to MoS_2, is stacked mono-layers of S-W-S units via van der-Waal forces. A single unit cell has a lattice constant of "a"=0.3153 nm and "c" = 1.2323 nm according to [8].

2.4.2   Band Structure

Up until the year 2001, not many experimental band structure for WS_2 had been procured [8], though, Klien *et al.* conducted both simulations and experiments to characterize WS_2. In bulk, the system shows an indirect band-gap of 1.34 eV (experimental results, [34]) as shown in Figure 2.11a. For a single layer system, WS_2 shows
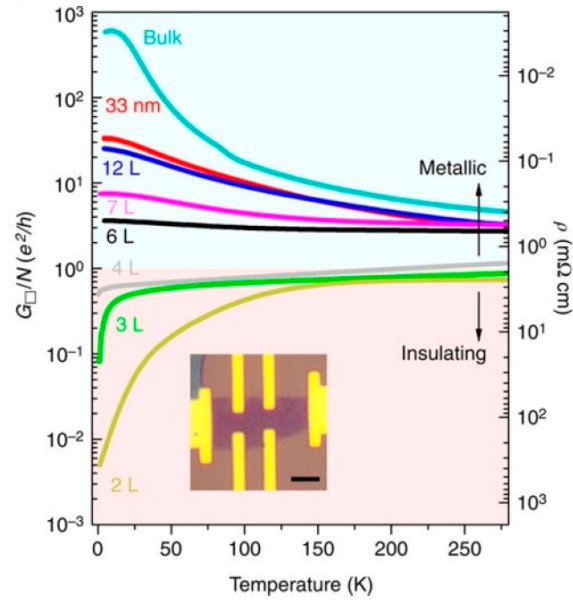
(a) Transition of WTe$_2$ from metallic to insulating.
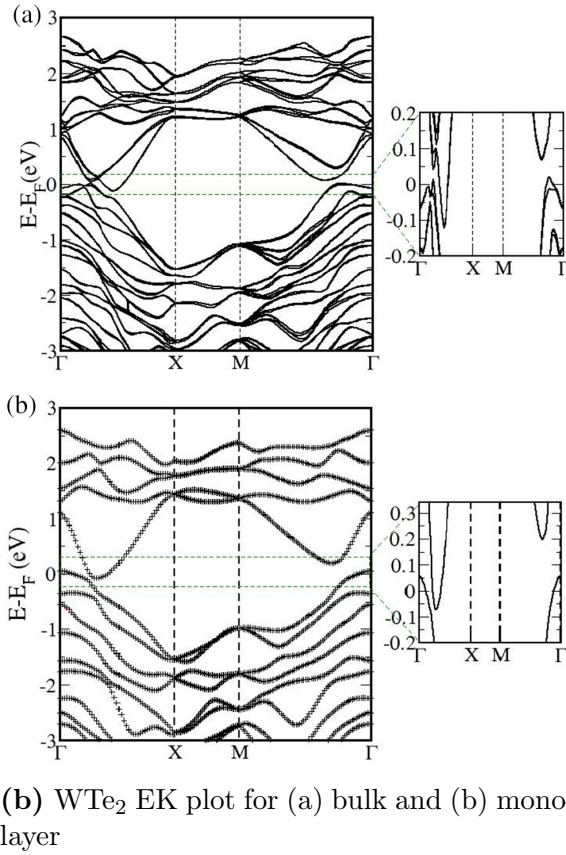
(b) WTe$_2$ EK plot for (a) bulk and (b) monolayer

Figure 2.9: Transition of WTe$_2$ from metallic to insulating as presented by [7]
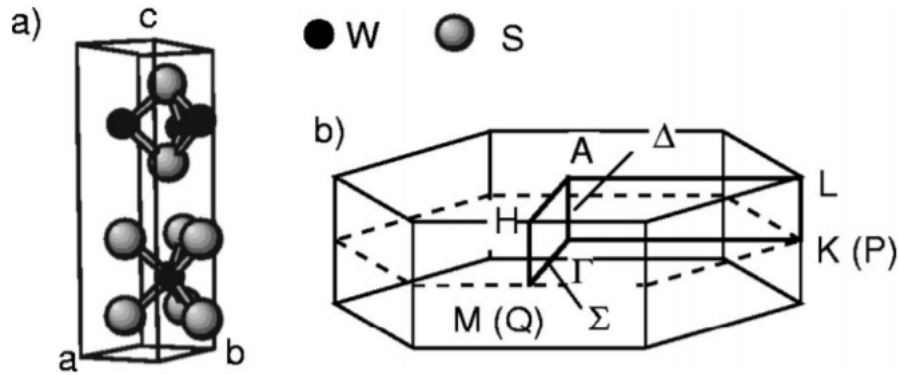
Figure 2.10: Crystal structure and Brillouin zone for WS2 [8]

an indirect band-gap of 1.6eV, Figure 2.11b. Very scarce literature is available on experimental results of the characterization of single layer and therefore band structure of WS_2 monolayer is under research.For instance in [35], Gusakova *et al* did an elaborate study on electronic structures for four TMDs (MoS_2, $MoSe_2$, WS_2, and WSe_2). It quotes monolayer of WS_2 to behave like a semiconductor with a band-gap of 2.03 eV [35]. A difference of 0.5 eV in band-gap is a large value to disturb the consensus and therefore calls for more research to be conducted for electrical properties of WS_2.

There has been very limited literature simulations for WS_2 and WTe_2 band structure using the hybrid functional like HSE06. Such a study would be an interesting extension to this project.

2.5 Chapter Summary

This chapter was intended to provide a description of electronic structure of transition metal dichalcogenides (TMDs) using example of three specific TMDs; one very heavily researched and the other two with enough empirical and experimental data to see their potential as promising novel materials. MoS_2 is discussed elaborately as it is studied in detail in this project as well. MoS_2, as various literature quotes, shows a transition
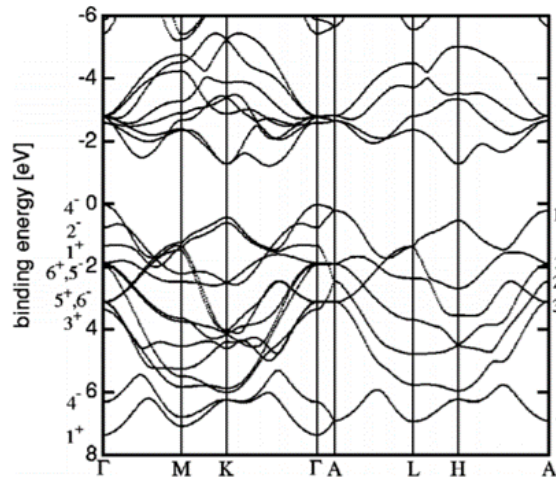
(a) E-K plot for WS$_2$ bulk
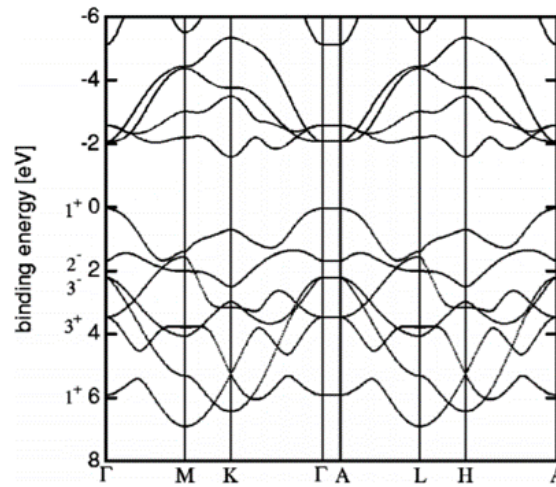
(b) E-K plot for WS$_2$ bulk

Figure 2.11: Band-struture of WS$_2$ as given by [8]

from indirect band-gap system to a direct band-gap seen at **K** k-point in Brillouin
zone. Unique magneto-resistive properties were seen in WTe$_2$ and an interesting
transition from highly conducting to insulating is seen when the system transitions
from bulk to single layer respectively. The brief introduction presented shows, WTe$_2$
is not yet found to be a suitable semiconductor for field-effect devices but shows the
great ability for tuning band-gap. This chapter introduces basic material properties
for molybdenum disulfide, tungsten di-telluride, and tungsten disulfide.

Chapter 3

Device Physics: Tunnel Diode, TFET and Heterojunctions

3.1 Introduction

In a classical semiconductor device operation, the charge carriers gain energy to go over the potential barrier created by the dopant concentration junction. Tunneling devices on the other hand do not require the charge carriers to gain that much energy. If the energy barrier is sufficiently thin/narrow, the charge carriers can tunnel through the barrier. The potential energy and the momentum of the incoming wave dictates the probability of wave transmission through the barrier. The potential energy (as in classical physics) is dependent on the mass of the charge carriers (electron and holes). Therefore, the heavier the effective mass (i.e., the mass of electron/hole when under external forces like an electric field), the lower will be the tunneling probability, as shown by equation 3.1. The equation presents the transmission probability of an electron wave, obtained from the WKB approximation [36].

$$T = \frac{exp(-2\int_{x_1}^{x_2} dx\sqrt{\frac{2m}{\hbar^2}(V(x)-E)})}{(1+\frac{1}{4}exp(-2\int_{x_1}^{x_2} dx\sqrt{\frac{2m}{\hbar^2}(V(x)-E)}))^2} \qquad (3.1)$$

Here m is the effective mass and the denominator factor is squared, therefore effective mass has a higher impact on the transmission coefficient. The transmission probability, therefore, depends on the width of the tunneling window, i.e., in classical terms, how much distance the wave will have to travel before it is on the other side of the barrier. This factor is governed by the energy difference: $(V(x) - E)$. The equation 3.1 assumes that V(x) > E. The derivation of transmission coefficient through the WKB approximation is technically dense and for the simplicity of this document, it is not discussed in further detail.

Nonetheless, all the important details needed to understand the operation and architecture of the tunnel diode and tunnel field-effect devices are discussed in the following sections.

3.2 Tunnel Diode Theory

Tunnel diodes were discovered by Esaki in 1958 [37] when he saw an anomalous current in a degenerately doped germanium p-n junction. A typical tunnel diode is comprised of an abrupt p-n junction which is degenerately doped on both sides. The heavy dopant concentration on both sides causes the Fermi levels for both sides to reside inside the allowed bands. In these devices, the Fermi energy level of the n-side lies at least a few kT/q above the conduction band edge and the Fermi energy level on the p-side lies at least a few kT/q below the valence band edge. With extreme levels of degenerate doping, the Fermi level can be significantly farther than kT/q from the band edges. In the absence of external bias, an occupied state at a given energy level on the n-side corresponds energetically to an occupied state on the p-side; likewise, an unoccupied state at a given energy level on the n-side corresponds precisely to an unoccupied state at the same energy level on the p-side. Due to high dopant concentration, the energy barrier in the depletion region between the n-type and the p-type regions is very narrow in comparison to the conventional p-n junction

[38]. If this dimension is less than the deBroglie wavelength for the material (on the order or less than 100 $\mathring{A}$), tunneling may take place.

When the tunnel diode is reverse biased with the n+ side at a higher potential in comparison to the p+ side, the relative energy position of the conduction band edge of the n-type region (E_{Cn}) to the valence band edge of the p-type region (E_{Vp}) decreases as the E_{Cn} lowers with respect to E_{Vp}. This allows increased probability of tunneling of holes from p-side to n-side leading to a monotonic increase in current in the reverse direction, as shown in Figure 3.1a (b). When the diode is slightly forward biased, E_{Cn} moves up with respect to E_{Vp}. On the either side of the junction, there are a few electrons (filled states) above the Fermi level and a few holes (empty states) below the Fermi level. When the diode is further forward biased, the conduction band of the n-doped side gets aligned to the unoccupied states present on the p-doped side, thereby opening a tunneling window (Figure 3.1a (c)).

When the voltage reaches V_P (Figure 3.2), the energy band overlap offers the maximum number of occupied states on one side to be aligned to the maximum number of unoccupied states on the other side thereby providing the maximum tunneling current. On further increasing the voltage in the forward bias beyond V_P, the two bands get misaligned. Now the conduction band edge on one side starts to surpass the valence band edge on the other side. Therefore, the tunneling current starts to decrease.

The phenomenon of decreasing current with an increase in voltage is known as negative differential resistance (NDR) and it is the key characteristic of a tunneling device. NDR indicates the voltage range in which the tunneling window exists. Once the conduction band edge completely crosses over the valence band edge, we see an increase in current again. This current is now diffusion current; the charge carriers (here electrons) have enough energy to overcome the energy barrier to reach the other side rather than by tunneling through the barrier.
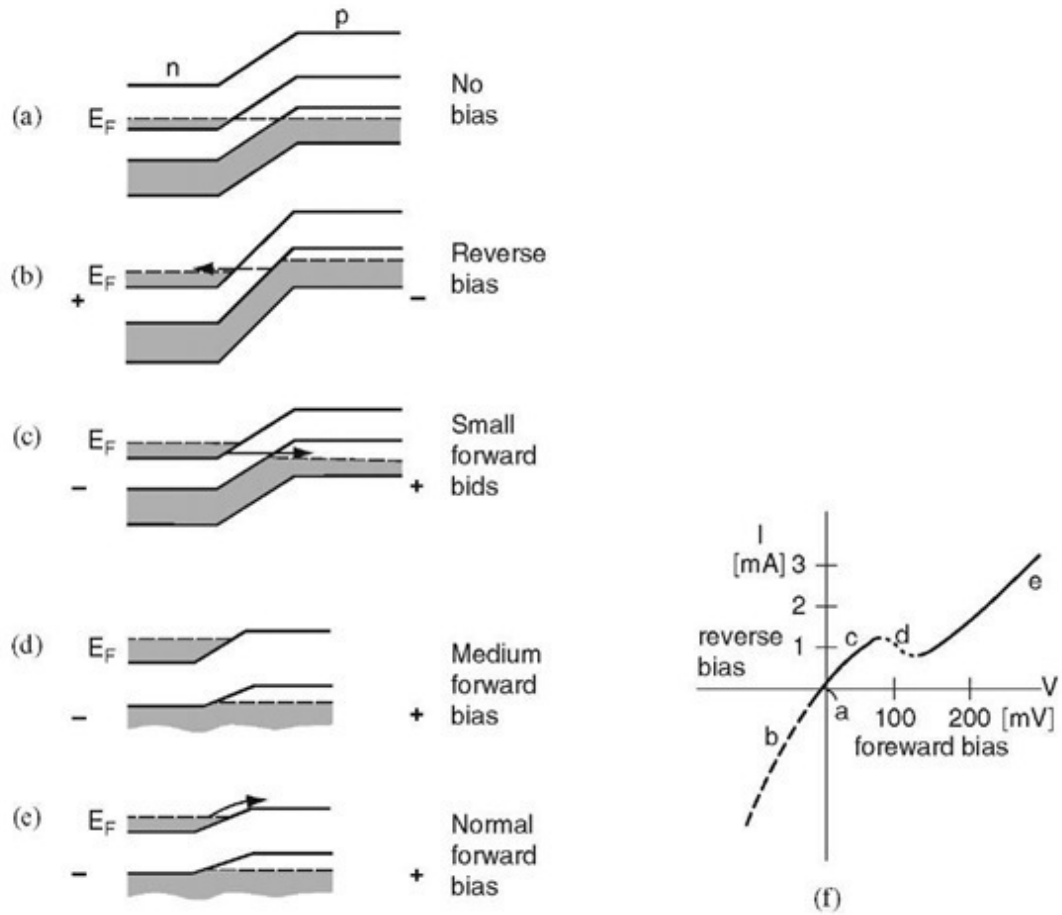
(a) Energy band explanation of tunnel diode operation [9]
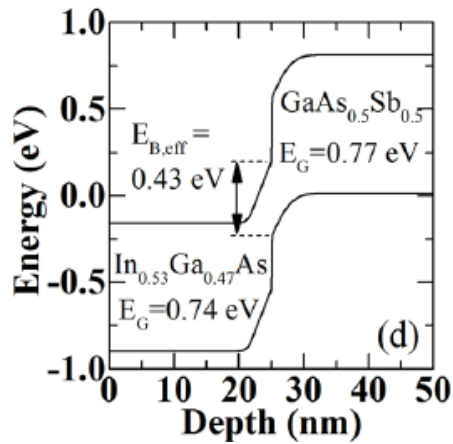
(b) E_f [10]

Figure 3.1: (a)graphical depiction of band energy of tunnel diode at different biases [9] (b)Effective band gap (E_f) in InGaAs-GaAsSb heterojunction tunnel diode[10]
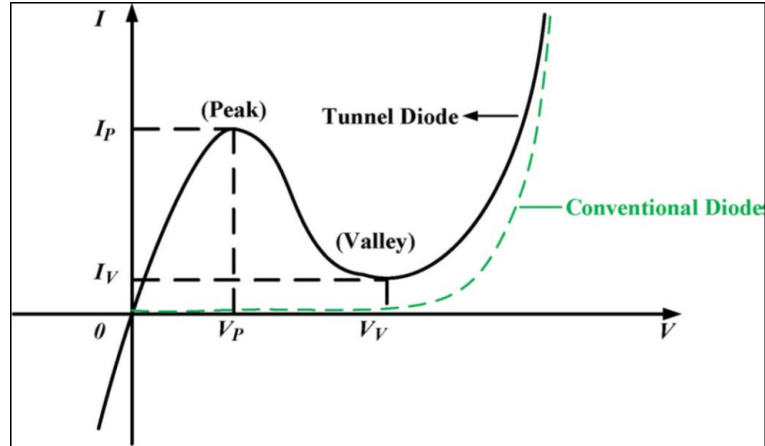
Figure 3.2: Negative Differential Resistance shown in tunnel diodes vs diffusion current in conventional diodes [11]

3.3 Tunnel Field-Effect Transistors

Conventional field-effect technology is limited by field-driven and diffusive charge transport. It primarily relies on the modulation of thermal emission of charge from source contact to drain contact via the channel region, controlled by gate voltage (V_g) and supply/drain voltage (V_d). The subthreshold swing for a MOSFET is given by equation 3.2

$$SS = (1 + \frac{C_{dep}}{C_{ox}})\frac{kT}{q}ln(10) \tag{3.2}$$

Since the depletion capacitance and the oxide capacitance in a MOSFET will always be positive, the minimum value for the given SS will be limited to 60 mV/dec at room temperature. Therefore, in order to obtain smaller subthreshold swing, the device operation needs to be independent of ambient temperature. This requirement is fulfilled by tunneling field-effect transistors (TFETs). TFETs are steep subthreshold swing transistors in which the charge transport is carried out via band-to-band tunneling (BTBT) between source and channel. The device architecture consists of degenerately doped source and drain regions that sandwich an intrinsic region. The

source and channel regions are doped with contrasting dopant types, i.e., if the source
is n-type doped then drain would be p-type doped or vice versa.
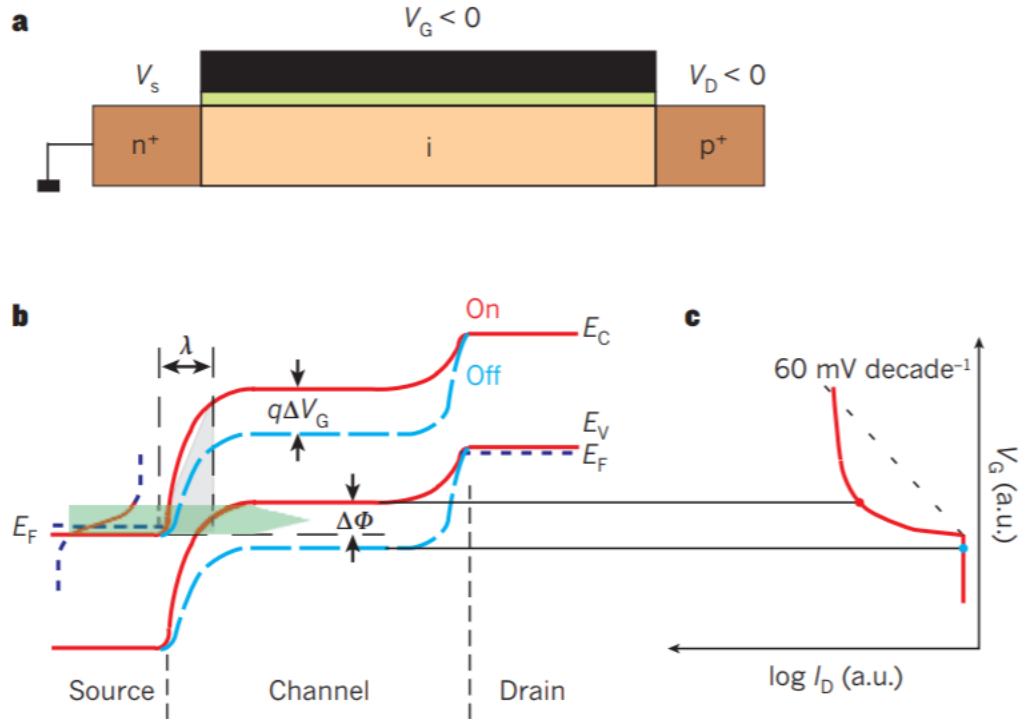
Figure 3.3: (a) TFET device schematic (b) Band bending in a TFET when under bias
(c)Change in I_D with changing gate voltage (V_G) in comparison to MOSFETs [12]

Figure 3.3 is a schematic showing the principle of operation of a typical n-i-p TFET
[12]. In the off state (dashed line in the figure), the conduction band edge of the source
is below the valence band edge of the channel, therefore the probability of tunneling is
small. Furthermore, since the junction between the source and the channel is abrupt
and the potential barrier between them is high either due to degenerate doping or
difference in materials, there is negligible diffusion current. This ideally leads to
a small leakage current in off state (i.e. small I_{off}). On applying a gate voltage
(negative in the given case), the channel region bands are pulled up just enough to
bring the conduction band of the source in line with the valence band of the channel,
thereby opening a tunneling window for Zener tunneling. The opposite doping at the
drain end permits a seamless path for charge carriers to be driven out of drain region

as the valence band of drain lies above the valence band of the intrinsic region (in the presented case) leading to drive current.

Drive current in a TFET is critically dependent on the tunneling probability of charge carriers through the inter-band tunneling barrier. The tunneling probability, given by equation 3.3, is obtained by approximating the tunnel barrier to be a triangular boundary barrier and then using WKB approximation [12]. WKB approximation is known to work appropriately for only direct band gap semiconductor devices, like InAs, but for indirect semiconductor tunneling FETs like those made from silicon or germanium, the WKB approximation shows limited accuracy [12]. Equation 3.3 gives the expression for transmission probability without including phonon scattering.

$$T_{WKB} \approx exp(-\frac{4\lambda\sqrt{2m*}\sqrt{E_g^3}}{3q\hbar(E_g + \Delta\Phi)}) \tag{3.3}$$

where m^* is the effective mass of the charge carrier, E_g is the bandgap, $\Delta\Phi$ is the energy gap between conduction band of source and valence band of channel (like an energy window), and λ is the effective tunneling length. Here λ is described by the spatial extent of tunneling region at the source-channel interface, as shown in Figure 3.3 (b). For a TFET at constant V_D, λ depends significantly on the value of V_G. On increasing V_G, value of λ reduces indicating an increase in the energy difference between the conduction band of source and the valence band of channel. This shows a significant influence of V_G in the initial approximation of drain current [12].

This exponential dependency of drain current on V_G shows that, unlike in MOSFET, in a TFET the subthreshold swing's dependence on the gate voltage is neither linear nor a constant value. Thus in a TFET, scaling down the gate voltage scales down the subthreshold swing without increasing the leakage current, therefore maintaining the device's performance. To obtain a significant drain current from a tunneling device, the tunneling probability should be aimed at being close to unity.

As equation 3.3 suggests, in order to bring T_{WKB} closer to unity, the device system should have a minimized value of m^*, E_G and λ. Here, m^* and E_G can be minimized by choosing the appropriate material systems. Lamba (λ) on the other hand can be controlled by geometric factors of the device, doping profiles and improved gate control. High gate control can be attained by high dielectric (high-κ) and thin gate oxide. To minimize λ the body thickness should also be minimized.

Ideally a one-dimensional body will provide the minimum body thickness and therefore a small value of λ. Thus, with lowering both off current and supply voltage (V_{DD}), a TFET device can reduce the operating power of the system significantly.

For a TFET to operate efficiently, the following two conditions are required:

- A thin enough barrier for charge carriers to tunnel through spread over large area to produce substantial current.

- Enough density of states in both the reservoirs and channel to provide energy sites for carriers.

The following chapter discusses atomistic modeling theory which provides information about the numerical models that can be used to estimate the electronic characteristics of a material from an atomistic stand point. The folowing chapters discuss the means of calibrating materials that can be used as one-dimensional channel material for TFETs and other tunneling devices.

Chapter 4

Theory of Atomistic Modeling

This chapter is the basis for the undertaken project, i.e. atomistic simulation of tunneling devices. Simulation of any device starts with a process of defining the working environment, identifying the variables and constants, and then developing modeling equations to simulate the system operation. The environment definition consists of the modeling of the material, setting up the crystal structure and the thickness of material along with other material properties. These parameters are then used in calculating the energy-momentum relationships (in k space) for the system in consideration, which defines the band structure of the material. Band structure of a material provides the characteristic information about the system such as the range of a device's operating voltage, mobility of charge carriers, magnetic and optical properties of the material and the density of states of the charge carriers in low energy valleys.

Atomistic modeling of a device holistically consists of two processes: first, calibration and characterization of the material, followed by characterization of carrier transport for the device of concern. The material is studied for its electronic structure and optical properties using numerical models that quantify the effect of inter-atomic forces. Charge transport in an electric field is highly dependent on the length of the device, i.e. distance to travel. The following sections provide an insight into the explanation and algorithm flow (where applicable) for different models used in

electronic characterization and charge transport in a device under bias.

4.1 Numerical Models for Material Characterization

To estimate the electronic properties of a material, one needs to obtain the complete solution of Schrodinger's equation. For any material, the electronic property is estimated by the analysis of energy-momentum $(E - k)$ plot which contains the location of the least energy valley points where the majority of the electrons reside. The Schrodinger equation (SE) provides the total energy of the system and for a single electron system as shown in equation 4.1.

$$\hat{H}(x)\phi(x) = \frac{-\hbar^2}{2m}\frac{d^2\psi(x)}{dx^2} + V(x)\psi(x) = E\psi(x) \qquad (4.1)$$

where $\hat{H}$ is the Hamiltonian operator, $\hbar$ is the reduced Planck constant, $\phi(x)$ is the state vector of the system, m is the effective mass of the charge carrier, $\psi(x)$ is the position space wave function, $V(x)$ is the potential energy variation along the x-axis of the electronic system and E is the energy level of the barrier.

Solving SE for a single electron body is doable, but for all practical purposes, SE needs to be solved for a multi-electron system, which is extremely complicated to solve. Thus the problem statement is simplified by using approximations and system boundaries. Different methods to solve Schrodinger's equation are categorized on the basis of their accuracy versus the computational time to reach an acceptable solution. The solution is primarily approached through Born-Oppenheimer approximation for nuclei motion [13].

Born-Oppenheimer approximation initiates a reduction of degree of freedom to solve Schrodinger's equation. The approximation suggests neglecting the velocity of nucleus and states that the wave function will depend on the position of the nucleus but not the velocity [13]. One of the widely used methods is known as Density
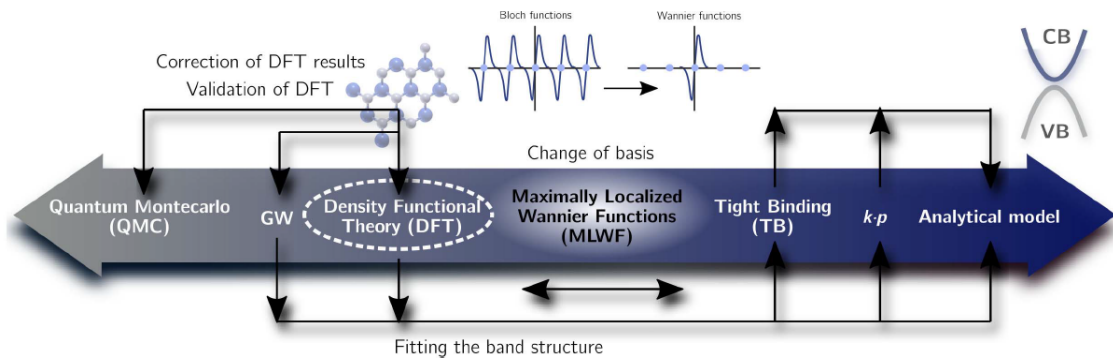
Figure 4.1: Hierarchy of computational methods arranged according to accuracy and computation expense [13] (a)Left: High accuracy and high computational expenses (b) Right: Low accuracy and low computation expenses

Functional Theory (DFT) and is discussed in the following section.

4.1.1 Density Functional Theory

What is Density Functional Theory?

Density Functional Theory is a simplification method of solving the Schrodinger equation for a multi-body system, by solving a fewer-variable electron density function to get total energy of the system. The interactions influencing the system's operation in a multi-body system are:

- electron-electron interaction

- electron-nucleus interaction

- nucleus-nucleus interaction

- kinetic energies of electron

- kinetic energy of nucleus

In order to obtain the total energy of a system such described, one has to solve the SE accounting for each of these interactions for all the electrons present. This is more than just tedious. A million-variable SE equation is impractical to solve explicitly.

Therefore, among other approximated methods to solve for a multi-body system, DFT (density functional theory) is one of the most exploited theories. Using Born-Oppenheimer approximation, one neglects some of the smaller-impact interactions in a system like that of one nucleus on another. It neglects the dependency of the nucleus velocity and considers only its position as a valid variable in the equation. With this approximation in place, the kinetic energy for nucleus and kinetic interaction between electron and nucleus can be safely ignored. The only interaction now valid regarding nucleus is the coulombic interaction between the electron and nucleus and the position of the nucleus. This approximation seems computationally safe as the mass of the nucleus in comparison to an electron is very high, therefore the velocity tends to be very small in comparison to the electron. It is safe to say that they are stationary relative to electrons [13]. Such an approximation leads to a large reduction in the number of variables that need to be solved for.

Born-Oppenheimer relation is position-dependent and therefore largely depends on what system is being solved, the molecular structure, the lattice orientation and resulting electron affinity of the molecule under consideration. While solving DFT, this factor is considered as an external potential, therefore can be included in the equation as an additive expression.

Another approximation employed in solving DFT was presented by Kohn-Hohenburg in 1964 [39] and converted to approximation methods by Kohn-Sham [40] in 1965. It states that the total energy of the system in its ground state shares a one-to-one relation with the electron density functional of the system. Therefore, if we know the electron/particle density of the system at the ground state, we know the total energy of the system at ground state as well. Kohn-Sham developed a set of self-consistent equations where the exchange potential/energy and the correlation potential/energy appeared as additive potentials [40].

With all the approximations decided, now it is important to understand how

DFT is computationally solved in order to get the solution (approximate solution) to Schrodinger's equation for a multi-electron system.

Method of solving DFT

The solution to DFT was proposed by Hohenberg and Kohn in the form of two theorems. The first theorem implies that the expectation value of any many-electron system in the ground state is a function of its electron density (ρ), given by Eq. 4.2. The second theorem extends the first theorem in saying that the ground state energy (E_0) of a system will be in correspondence to the ground state electron density ρ_0, given by Eq. 4.3. This suggests that if one knows the ground state electron density of a many-electron system, one can directly obtain the energy states of the system, without going through the tedious/impossible calculation of solving the Schrodinger equations for many-electron wavefunctions. Now, one can use variational principal to calculate the minimum of the total energy functional, E_0 which will be correlated to the ground state electron density.

$$\rho(r) = \sum_i |\phi_i(r)|^2 \tag{4.2}$$

$$[\frac{-\Delta^2}{2} + V_{KS}]\phi_i(r) = \epsilon_i \phi_i(r) \tag{4.3}$$

A system consists of interacting and non-interacting particles. Equation 4.3 gives the variational principle Kohn-Sham equation that is used to transform multi-electron system to single-electron system.

Kohn-Sham described these equations for a hypothetical system (called the Kohn-Sham system) consisting of non-interacting electrons, which had the same density as that of a system with interacting electrons. The impact of the interaction with other electrons in Kohn-Sham system was expressed as an external potential. This external potential is known as the exchange-correlation potential V_{ex}, shown in Eq. 4.4.

$$V_{KS}(r) = v(r) + v_H(r) + v_e x(r) \qquad (4.4)$$

where $v_H(r)$ is the Hartree Potential and $v_e x(r)$ is the exchange-correlation potential. Identification of the exchange-correlation potential dictates the accuracy and also the computational cost of solving the set of equations. Third party simulator systems like VASP (Vienna *ab initio* Simulation Package) and ATK (Atomistic Tool kit) have been programmed to solve these equations depending on what exchange-correlation function is being chosen by the user. These correlation functions were studied and arranged in the order of simplicity and accuracy by JP Perdew and K Schmidt in their famous publication [14] Figure 4.2, known as Jacob's Ladder.
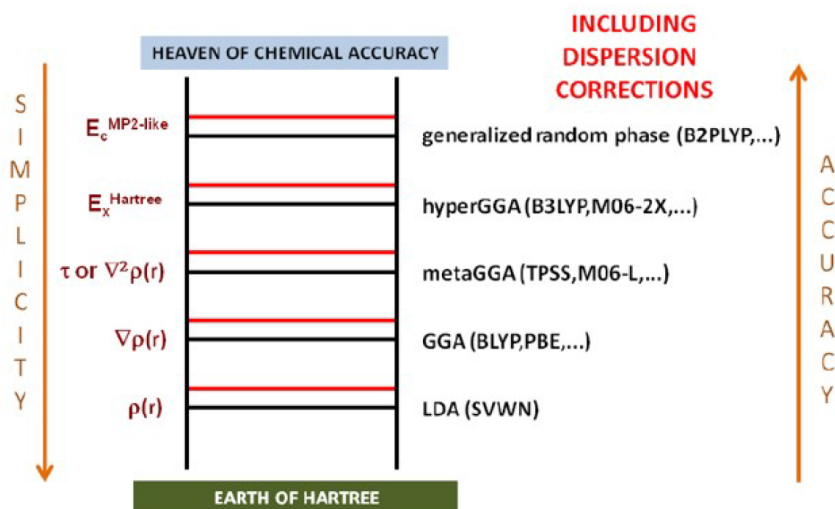
Figure 4.2: Jacob's ladder [14, 15]

The ladder shows different approximations that can be considered, depending on the requirement of the system and the availability of resources. As it shows, Generalized Gradient Approximation (GGA) and metaGGA utilize double gradient of electronic density, therefore normalize error that might be observed when calculating using only the density, like in Local Density Approximation (LDA). The computation accuracy is acceptable for GGA and so is its computational time consumption. As we will see below, majority of the studies carried forward for these simulations have used

GGA with PBE. HSE06 is another option, which is a hybrid of GGA and Hartree-Fock formalism. It shows much higher accuracy than any other (apart from quantum Monte-Carlo [13]) approximation, but the computational time and power consumed in a simulation using HSE06 is way too large.

4.1.1.1   Hybrid Functional

Hybrid functional is a combination of discrete and exact exchange function from Hartree-Fock theory and an exchange-correlation function from ab-initio or empirical study. This is aimed to maintain a mean between the two methods thereby minimizing the extreme anomalies. Meta-GGA (Meta Generalized Gradient Approximation) and HSE06 belong to the category of hybrid functional. The choice of functional to be used primarily depends on the kind of system at hand and the computational power at hand. With respect to TMDs, there is a dire need for bench-marking HSE06 like hybrid functional using different TMD materials. As we will see later in results, even though research and experiments have shown HSE06 to be very accurate when used for III-V systems or other semiconducting systems [15], we see it overestimates the band-gap when used for monolayer MoS_2.

4.1.2   Van der Waals forces in DFT- vdW-DFT

For material systems that exist in the form of stacked layers held together by van der Waal forces, DFT that incorporates the van der Waal forces is also developed. The local and semi-local functionals like local density approximation and gradual gradient approximation do not account for the weak van der Waal forces that arise due to fluctuating charge distribution between two non-bonding layers. In order to incorporate these forces in DFT calculations, a correction factor is added to the Kohn-Sham DFT energy equation as shown in equation 4.5 [41].

$$E_{DFT-disp} = E_{KS-DFT} + E_{disp} \tag{4.5}$$

In equation 4.5, E_{KS-DFT} refers to the Kohn-Sham energy approximation and E_{disp} is the non-local dispersion energy functional that incorporates the van der Waal's forces' effect. E_{disp} correction factor in equation 4.5 is computed by using different approximation methods which are non-local functionals [41]. VASP module provides the option to use about seven types of these non-local dispersion energy approximations. All the approximations add van der Waal correction to potential energy, inter-atomic forces and stress tensor. Therefore simulations involving lattice relaxation, molecular-dynamics, and vibrational analysis can be performed keeping van der Waal's forces into consideration.

4.2   Charge Transport Model Theory

For an operational device, the system's reaction to an electric field needs to be analyzed. Once the dimension of the device's operational length becomes comparable to the lattice constant of the material, a quantum level analysis needs to be performed for electron distribution in a non-zero electric field. The process, at a high level, involves the inclusion of a link between external potential and charge carriers This link is enabled by the Poisson equation. Therefore all the transport mechanism solvers follow an input of electronic structure from the material characterization and use that input to solve for the Poisson equation to give potential in the device. This follows a self-consistent iterative process between this potential and a charge density obtained from one of the charge transport models (QTBM or NEGF). Once the error between two consecutive iterations reaches an acceptable value (like $1x10^{-3}$ or $1x10^{-5}$ eV), the system moves to next voltage point. Given below is a brief discussion on the two charge transport models.

4.2.1 Quantum Transmitting Boundary Method (QTBM)

What is QTBM?

Quantum transmitting boundary method was developed by Lent in 1990[42]. It is a generalized numerical algorithm developed to calculate the complete solution of Schrodinger equation in the device region using boundary conditions appropriate for two-dimensional charge transmission, also known as "current carrying states" or "scattering states" [42]. QTBM's specific focus is in obtaining a solution to Schrodinger's equation for open boundary device region under non-equilibrium potential. The algorithm when first conceived was solved for a system partitioned into a device region and a contact or leads region, which extended to infinity [42]. The boundary conditions are formulated such that the device is discretized using finite element method, which is connected to leads on left and right, Figure 4.3.

The process of breaking the system into discrete mesh nodes makes the calculation of wave equation less complex as we would see in brief below. Generally, in a continuous system, meshing can be done according to some pre-defined symmetry points. In an atomistic system, the mesh nodes are set according to the location of atoms, which is why the information about the lattice structure of the material under study is of prime importance. Otherwise, it becomes very counter-intuitive to perform a numerical calculation for a nodal point in places which in reality are a void.
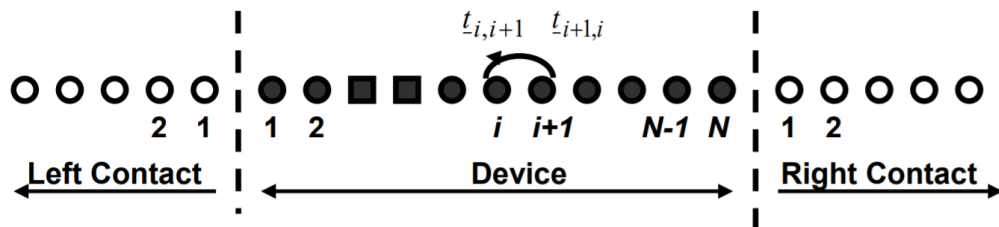
Figure 4.3: Graphical description of device discretization consisting of device, left contact and right contact [16]

Defined device does not have rigid boundary, i.e. $\psi_0(x_0) \neq 0$ and $\psi_N(x_N) \neq 0$. Such a system allows transmission through the boundaries where there is a constant injection from one reservoir (Source) and a consistent pumping out into the sink (Drain), which permits a constant charge movement through the device. QTBM functional is used to calculate the wave function through such an open boundary device structure connected to infinite or semi-infinite leads.

How is it solved?

The device region is meshed and solved for the non-equilibrium transport equations whereas the contacts are assumed to be at local equilibrium. QTBM involves solving of the system of linear equation given by equation 4.6 ([42]).

$$(\mathbf{T} + \mathbf{V} + \hat{\mathbf{C}})\mathbf{u} = \hat{\mathbf{P}} \tag{4.6}$$

where $\mathbf{T}$ is the discretized shape function (mxm) matrix for the device with m nodal points. $\mathbf{T}$ can be obtained from equation 4.7

$$T_{i,j} = \frac{\hbar^2}{2m^*} \int_{\Omega_0} [d_x\phi_i(\mathbf{r})d_x\phi_j(\mathbf{r}) - d_y\phi_i(\mathbf{r})d_y\phi_j(\mathbf{r})]d^2r \tag{4.7}$$

Each of the "m" nodal point's shape function has its associated wave function approximation given by equation 4.8:

$$\Phi_0(x) = \sum_{i=1}^{2} \Phi(r_i)\phi_i(r) \tag{4.8}$$

Similarly $\hat{\mathbf{V}}$ present in equation 4.6 is also a *(mxm)* matrix of discretized potentials across all 'm' shape basis functions as given by equation 4.9:

$$V_{i,j} = \int_{\Omega_0} [V(r) - E]\phi_i(r)\phi_j(r)d^2r \tag{4.9}$$

The LHS of QTBM equation (eq. 4.6) consists of the isolated device Hamiltonian with self energy from the two contacts (here, i and j refer to the two reservoirs/contacts). The self energies can be obtained from the transfer matrix method where a generalized eigenvalue problem solves for contact modes and these contact modes get translated into a surface Green's function and self energy. NEMO5 optimized this attaining of self energies by some simplifications like using only real-valued operations (for nanowires) and conversion of generalized eigenvalue problem to the normal eigenvalue problem. These simplifications cut down the computational time dramatically [43]. For instance, the right hand side of the QTBM equation (eq. 4.6, gives the injection of charge carriers from the given reservoirs/contacts, and depends on surface Green's function, contact propagating modes and the propagation phase factor. As a simplification, NEMO5's algorithm has a rewritten version of RHS that does not rely on surface Green's function explicitly thereby speeding up the computation of RHS of the QTBM equation by 35 times in comparison to the direct solution [43].

$$RHS \sim -\sum^{R} \Phi_P e^{-ikp\Delta} \tag{4.10}$$

This led to a speed up of 35 times the original speed, which is extremely useful given the complexity of the original algorithm given by Lent [42].

4.2.2 Non-Equilibrium Green's Function (NEGF/RGF)

What is NEGF?

NEGF, like QTBM, is a methodology to solve for the charge density and current in the conductor region of the device when it is under bias, like solving Schrodinger equation for wave functions for an open boundary system operating in ballistic regime. The main difference between QTBM and NEGF is the inclusion of scattering in NEGF and not in QTBM, causing an added computational expense in solving NEGF. The

complete solution to transport model is still solved self-consistently, but now it is between NEGF (for charge density) and Poisson equation (for potential). In solving for the charge transport between two reservoirs that are not in equilibrium, NEGF forms an interconnect between the two using self-energy functions. Below a short description of solving transport model using NEGF is presented.

How is it solved?
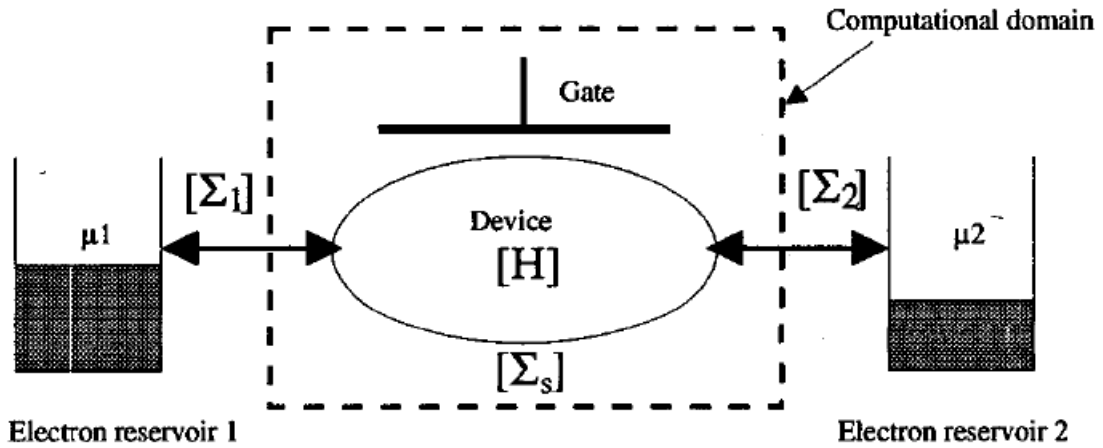
Figure 4.4: Schematic of computational system with reservoirs under non-equilibrium, [H] has Hamiltonian of device, self energies associated with contacts($[\sum_1]$,$[\sum_2]$) and scattering self-energy ($[\sum_S]$) [17]

Given the Hamiltonian matrix for an infinite device region [H], shown in Figure 4.4 and given energy E, the Green's Function is given by [17, 44]:

$$(E - H)G(x, x`) = \delta(x - x`) \tag{4.11}$$

Here the Hamiltonian [H] is considered for an infinite system. But in reality, one needn't solve for an infinite system and instead convert it to an isolated system with Hamiltonian $[H_0]$ which is linked to the reservoirs via self-energies of reservoir "j" $[\sum_j]$, as shown in Figure 4.4. This leads to the formation of a retarded Green's function

(RGF) which is given by:

$$[G(E)] = (E[S] - [H_0] - \sum_j [\sum_j (E)])^{-1} \tag{4.12}$$

where [S] gives the identity matrix for orthogonal basis function which is used to discretize the system [17]. Next, the self-energy matrix $[\sum_j]$, which is of the same size as $[H_0]$, can be given by

$$[\sum_j (E)] = [\tau_j][g_j][\tau_j^+] \tag{4.13}$$

where $[g_j]$ is the surface Green's function for reservoir "j" and τ_j is the coupling matrix for the device and reservoir surface. The non-equilibrium density matrix can then be given by

$$[\rho] = \int_{-\infty}^{\infty} \frac{dE}{2\pi} \sum_j f_{FD}(E - \mu_j)[A_j(E)] \tag{4.14}$$

with,

$$[A_j(E)] = [G(E)][\Gamma_j(E)][G^+(E)] \tag{4.15}$$

and Γ_j, the broadening function as

$$[\Gamma_j] = i([\sum (E)] - [\overset{+}{\sum}(E)]) \tag{4.16}$$

But here in the charge density matrix, the diagonal comprises the electron density n, which is a function of potential U in the device. Therefore, to reach the point of getting the density matrix and charge distribution, equation 4.14 needs to be solved self-consistently with the Poisson equation, until a point of convergence is reached. Finally, the drive current between the two contacts in the given ballistic system can

be obtained from

$$I = \frac{2q}{h} \int_{-\infty}^{\infty} dET(E)(f_{FD}(E - \mu_1) - f_{FD}(E - \mu_2)) \qquad (4.17)$$

T(E) is the transmission coefficient which is given by

$$T(E) = Trace[\Gamma_1 G \Gamma_2 G^+] \qquad (4.18)$$

Under the umbrella of this general set of equations to solve for charge transport, some optimizations are further performed to reduce the computational expenses. One of them mentioned above is using the retarded Green's function which is the reduction of the full matrix Green's function into a sparse matrix with three rows filled diagonally leading to a large memory saving for each data point. Due to the inclusion of scattering, the computational time for NEGF is substantially large in comparison to QTBM.

4.3   Chapter Summary

In the presented chapter, a brief view of the numerical methods of transport models was provided. The shell algorithm flow is a self-consistent iteration between one of these models and Poisson equation. An initial guess is given using some semi-classical approach solved with the Newton-Raphson method. The NEGF method can also be discretized using Finite Element Method (FEM). The atomistic modeling tool NEMO5 employees RGF and QTBM for their charge density calculations. QTBM is a preferred model when dealing with monolayer and no scattering is observed when the system is 2D. This project is focused on devices consisting only monolayer materials systems therefore only QTBM was used for device simulations.

Chapter 5

Material Characterization using VASP and NEMO5

5.1   Introduction

Keeping the focus primarily on TMDs (transition metal dichalcogenides), simulations were performed to characterize the TMD materials available in the database of the tool, MedeA-VASP (called VASP henceforth) and NEMO5. NEMO5 allows one to override the default material parameters using commands while writing the input deck. VASP too provides with such capabilities via its graphic user interface. TMD material studied here are with a molecular configuration of MX_2, where "M" is to a transition metal, like molybdenum, tungsten (W) and "X" is a chalcogen, like sulfur, selenium, tellurium etc. Structurally a TMD molecule consists of a transition metal sandwiched between two chalcogens. When such molecules combine to form a unit cell, each unicell has a hexagonal surface as shown in Figure 5.1 [18].

The common sequence of steps followed in VASP simulations was to use their "infomatica" material database and search for the required material. The database gives out the available material systems within various space groups. To identify the most reliable system, we filter out the median of all the structures given and use the one with the highest value. This ensures, to an extent, that the material parameters are reliable. The obtained material is generally in 2-3 layer format, as shown in Figure 5.2a . We convert this structure to a monolayer by removing the extra layer
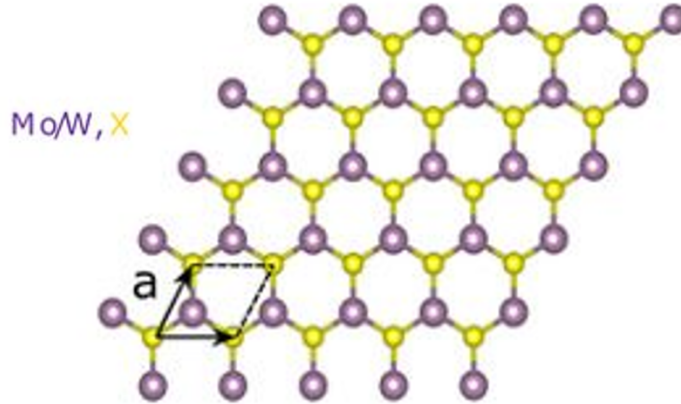
Figure 5.1: Structure of mono-layer TMD: top view. "a" is the lattice constant for given unit cell [18]

(literally deleting the atoms in VASP, a little strange idea, but the code behind it is strong enough to understand this "deletion", so does not give erroneous values). To ensure that the repeated layers do not interact with each other, we increase the height lattice parameter ("c") to 20-30 $\mathring{A}$ ("c" generally is about $12\mathring{A}$). The transition from bulk to monolayer does not explicitly change any bond-lengths or lattice parameters. Once the structure is set up, before simulating the band-structure, a structural relaxation/optimization is performed. This structural optimization relaxes the structure a bit to bring it to the lowest energy state. To validate that the resulting structure's lattice parameters are not altered during the structural optimization, we re-check the values and then re-submit the job to calculate the band-structure and density of states. We used plane-wave cut off of 500-600 eV and optimization limit between $1e^{-5}$ and $1e^{-3}$ eV. Optimization/convergence limit refers to the allowed difference between consecutive iterations.

For NEMO5 simulations for $E - k$, a similar approach was taken. Although, instead of mentioning the lattice constant "c" as 20-30 $\mathring{A}$, we designed the geometry

and domain of the sample such that negligible interaction is present between two consecutive layers. Here too, we first define the structure of the material, mention the tight binding parameter to be used for energy-band calculations and the value of lattice's atomic radii. Then the domain and geometry are decided, which, if the domain is fixed at 1x1x1, a monolayer structure could be achieved. The following section briefly describes the results obtained for each of the mentioned TMD materials, tool-based tweaks performed, tight binding models used, the k-space matrix used, and the band structure along the high symmetry points along with their respective energy gaps obtained from both the tools.

5.2 Molybdenum Disulfide (MoS2)

Molybdenum disulfide's most explored space-group configuration is p63/mmc (in 3D) and P6mm in 2D. This configuration is the result of a hexagonal structure of the primitive lattice in two-dimensional space with mirroring along two axes.

5.2.1 Crystal Structure and Band-Structure

The crystal structure of MoS_2 is best visualized using the GUI provided by MedeA. The structure shows sp^2d^5 hybridization, therefore allowing strong covalent bonding between the molybdenum molecule and sulfur molecules. Using this structure, we bring the symmetry down to P1 (primitive cell) to convert the bulk structure to a monolayer using the steps mentioned above. Figure 5.2 shows the before and after images of bulk to monolayer conversion. Before any calculations can be performed, we re-raised the symmetry of the system to p6m bringing it closest to a monolayer MoS_2.
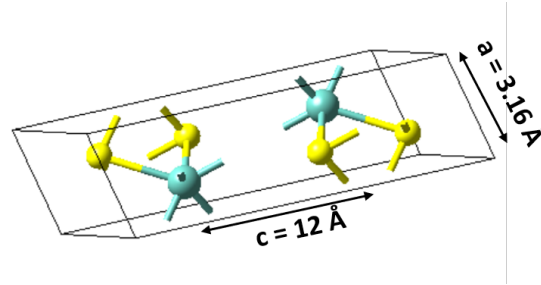
(a) MoS_2 VASP bulk
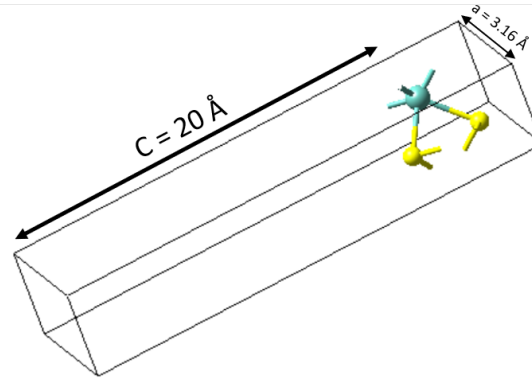
(b) MoS_2 VASP monolayer

Figure 5.2: Structure of MoS_2 (a) bulk, bilayer (b) monolayer, with lattice constant c = 20A

5.2.2   VASP simulation

MedeA-VASP was used to calculate $E - k$ plots and density of states for MoS_2. The first step towards band-structure calculation was cell relaxation. This enabled a stress-free structure for the crystal. The second step was to identify the path of high symmetry points in the Brillouin zone of MoS_2. MoS_2 is known to have an indirect bandgap in a bulk system, which translates to a direct band-gap when the system is thinned down to a monolayer. It should be noted that in a monolayer system, direct bandgap is observed at K k-point and not at Γ-K k-point. It is in the bulk system that one observes the minimum bandgap at Γ-K k-point point. A few references [19, 5] validate this observation. The k-point path, therefore, picked for this study was Γ-M-K-Q-Γ. Study of Brillouin zone shows the lack of band splitting at the given k-point path, therefore they are called points of high symmetry. The mentioned path

is the most common calculation path used in studies and therefore, to calibrate VASP and NEMO, this same high symmetry path was considered.

Another aspect of $E-k$ calculation is the k-space matrix. k-space matrix provides the simulator with the number of mesh points in the reciprocal space of the Brillouin zone. The effect of a different k-space matrix is:

1. Convergence of numerical models: for a dense mesh, a few failures in convergence points do not lead to incorrect results

2. On the negative side, a denser matrix leads to a higher computational time.

For simulations performed in this study, k-space matrices of 31x31x1, 7x7x1, and 20x4x1 were used. This matrix spacing is with respect to monolayer systems only. In the case of simulating bilayer systems, similar k-space matrices of 31x31x2, 7x7x2, and 20x4x2 could be used, or 31x31x5 for a bulk system with five layers. We investigated monolayers and bulk systems consisting of five layers. These matrices were used to replicate the system presented in literature for better comparison. There seems to be no consensus on the effect of the k-space matrix on the electronic structure of the material. To understand the effect, we tested different k-space matrices keeping other parameters identical. Figure (5.3) shows $E-k$ plots obtained from the test.

The observation of matrix-size test revealed a minor effect (but an effect nonetheless) on the band gap of the material. A matrix of 25x25x1 matrix size (without spin-orbit coupling) gave a band gap of 1.7 eV, which is closer to what a few references quote. The experiment does not show any linear relation with the matrix, yet the value is affected. Our best guess is that this is due to mesh convergence. But for this project, it still was an open question.

A final aspect of electronic structure simulation of a material is the tight binding models used to calculate the values. For this experiment, we primarily relied on density functional theory with GGA-PBEsol. Previous experiments [15] using III-V materials were performed to find out computationally accurate and optimal models for
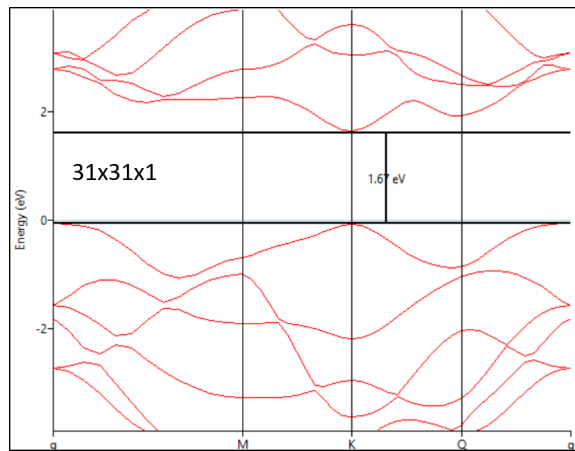
(a) band structure with k-space matrix of 31x31x1
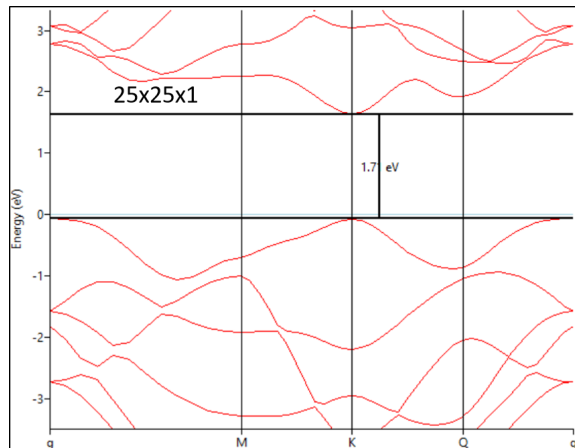
(b) band structure with k-space matrix of 25x25x1
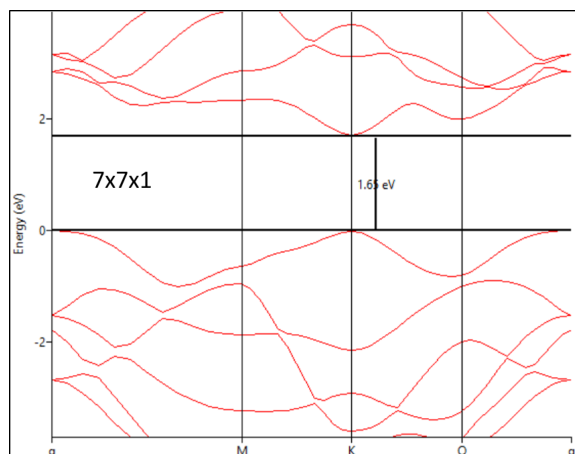
(c) band structure with k-space matrix of 7x7x1

Figure 5.3: Results of VASP k-space matrix experiment: band gap 31x31x1: E_g= 1.67 eV; 25x25x1: E_g= 1.71 eV; 7x7x1: E_g= 1.65 eV

material characterization. It has been found that even though HSE06 with GGA-PBE is more accurate, it is computationally expensive. Therefore, DFT with GGA-PBE is used with spin-orbit coupling kept in consideration. Figure 5.4 shows a comparison of $E - k$ plots for a monolayer MoS_2 system. The comparison is made between the work conducted by Kadanstev and Hawrylak in [19] and the simulations performed in this research using VASP tool. Kadanstev and Hawrylak used Kohn-Sham DFT functional to perform their simulations using a programming tool known as EXC!TING APW+lo program. The k-space matrix of 31x31x1 was used to sample the Brillouin zone of the single-layered MoS_2 system. The bulk unit cell of MoS_2 used by Kadanstev and Hawrylak belonged to the space group $P6_3/mmc$ and had lattice constants "a" equal to $3.122\mathring{A}$ and "c" equal to $11.986\mathring{A}$. The same system setup was used for this the VASP simulation performed in this research shown in Figure 5.4. The expected band structure for a monolayer system of MoS_2 is a direct bandgap at k-point K - K with value 1.79 eV, as per the cited literature [19]. Simulated plots show a bandgap of 1.64 eV at K - K zone boundary when calculated without spin-orbit coupling and a bandgap of approximately 1.9 eV when the simulation is performed including spin-orbit coupling.

Another simulation of band structure for MoS_2 was performed to compare results with the works of Gao *et al.* [5]. Gao *et al* used GGA-PBE variant of DFT functional and they included a correction factor for van der Waal forces (DFT-D2). Spin orbit coupling was not taken into consideration. The simulation included a monolayer system of MoS_2 with k-point sampling of 20x4x1 for the Brillouin zone. The same set up was used in VASP for this study in order to replicate the reference work and calibrate the material in VASP in doing so. The bandgap obtained for VASP simulations was found to be in agreement of the bandgap obtained by Gao *et al.*, which is equal to 1.8 eV as shown in Figure 5.5. This simulation work also showed the impact of including van der Waal correction factor (i.e., using vdW-DFT) when

(a) E-K of single MoS_2 monolayer [19] E_g 1.79 eV

(b) MoS_2 VASP without SOC; E_g 1.64 eV

(c) MoS_2 VASP with spin coupling; $E_g \approx 2$ eV
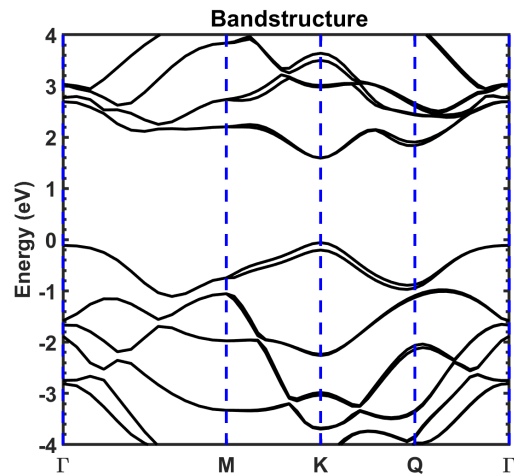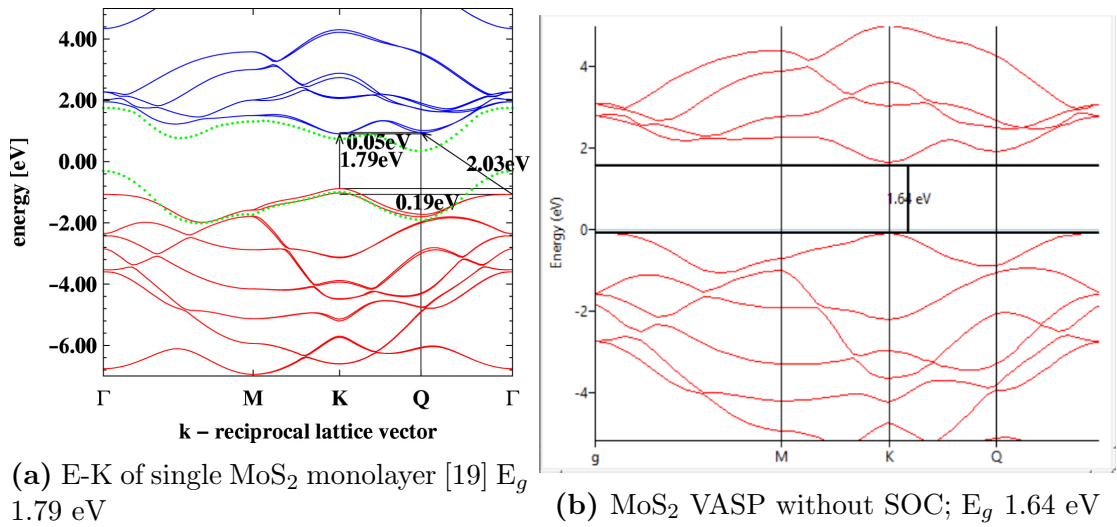
Figure 5.4: MoS_2 $E - k$ comparison between reference (work done by Kadanstev *et al.* [19]) and simulations performed using VASP; with and without spin orbit coupling inclusion

obtaining the band structure of a system like MoS_2.
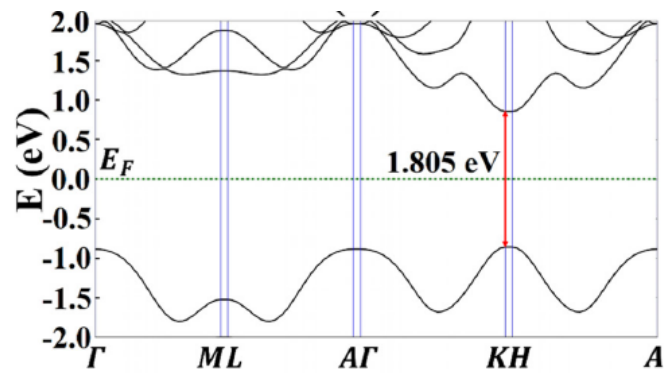
(a) MoS_2 VASP From Gao *et al.* [5]
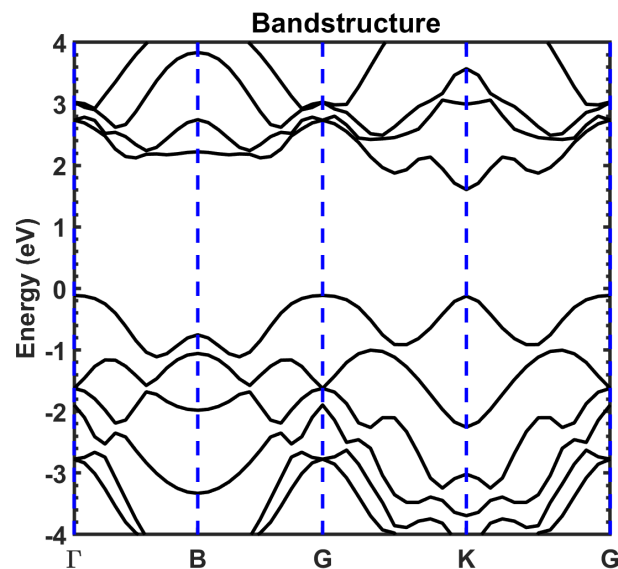
(b) MoS_2 VASP monolayer

Figure 5.5: Band structure comparison: MoS_2 VASP versus simulation conducted by Gao *et al.* [5]

Finally, a study was done to compare the difference between inclusion of spin-orbit coupling and without including spin-orbit coupling using a hybrid functional, HSE06 as shown in Figure 5.6.

The bandgap obtained from DFT-HSE06 with spin-orbit coupling is overestimated by 0.4 eV. Experimentally and via other DFT functionals, the bandgap for monolayer MoS_2 comes out around 1.8 eV. But this simulation gave a value of 2.2 eV. The reason for this discrepancy is unclear, even though HSE06 is known to be more accurate than

MoS$_2$ HSE06 Spin Orbit (solid)

MoS$_2$ HSE06 No Spin Orbit (dashed)
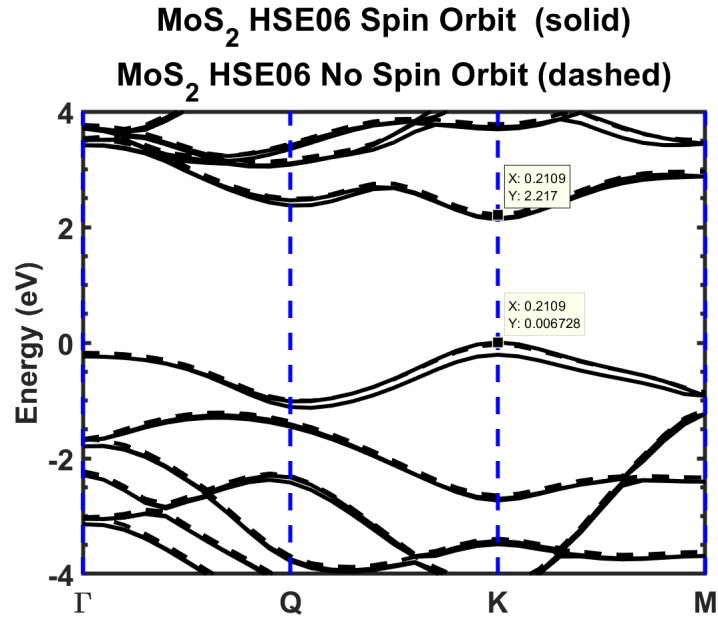
Figure 5.6: VASP simulation of MoS$_2$ bandstructure using DFT-HSE06

other functionals [15]. Further study in inquiring the cause of this result did not lead to a conclusion and proved computationally very expensive.

The run time for simulating MoS$_2$ with the spin-orbit coupling on a four-core system with no parallel processing was approximately two weeks. A slight error in the results was therefore obtained after two weeks of wait, which clearly is a huge computational road block. Since the time consumption proved to be such an important factor, a brief study was done to benchmark VASP for runtime using silicon, as silicon is the most common semiconductor and structurally not as complex as TMDs. Once VASP was bench-marked for silicon, similar values for KPAR and NPAR (two VASP parameters for parallel processing) were used for GaAs, InAs and MoS$_2$ to see the improvement.

Table 5.1 enumerates the obtained runtime for different materials after varying KPAR, NPAR and number of cores. In VASP module, NPAR and KPAR dictate the number of cores that will be used to run each band structure. By default, these values are equal to the number of cores requested and perform on a one-band-to-one-core

Material	Model	Cores	KPAR	NPAR	Run Time
Si	HSE06 with SOC	4	default	default	40 min
Si	HSE06 with SOC	6	default	default	30 min
Si	HSE06 with SOC	4	default	4	20 min 11 sec
Si	HSE06 with SOC	16	default	4	**6 min 57sec**
Si	HSE06 with SOC	25	default	5	18 min
Si	HSE06 with SOC	36	9	default	**6 min 40 sec**
GaAs	HSE06 with SOC + DOS	36	default	6	29 min
GaAs	HSE06 with SOC + DOS	36	9	default	15 min 40 sec
InAs	HSE06 with SOC	4	default	default	120 min
InAs	HSE06 with SOC	36	9	default	15 min 18 sec
MoS_2	HSE06 with SOC	4	default	default	2 weeks
MoS_2	HSE06 with SOC	36	36	default	2 days

Table 5.1: Table enumerating run time for different materials varying KPAR and NPAR. Bold numbers, lowest runtime for silicon.

basis. For MoS_2, the values are not optimized and since this experiment shows the drastic effect in cutting down run-time when the process is distributed across cores in an optimal manner, considering such a DOE on a larger number of materials and more number of experiments is suggested for a future experiment.

5.2.3   NEMO Simulations

NEMO simulation for material characterization gives a limited number of tight binding models to be explored. Most prominently used model is DFT with GGA. Figure 5.7 shows a comparison between the $E - k$ band structure obtained from NEMO5 with an $E - k$ plot obtained from VASP by Kadanstev and Hawrylak [19]. NEMO5 input deck allows one to set the k-point path. The output files obtained are data files of energy points, k points, and k distances. These can be plotted using either Origin, MATLAB or Python or any other plotter. For this research, MATLAB was used to plot the $E - k$ band structures of different material systems.

In NEMO5, MoS_2 was simulated along the high symmetry path that followed Γ-Q-K-M-Γ with 20 k-points (nodes) between two consecutive high symmetry points. The obtained output was normalized against the k-space in order to identify the zone
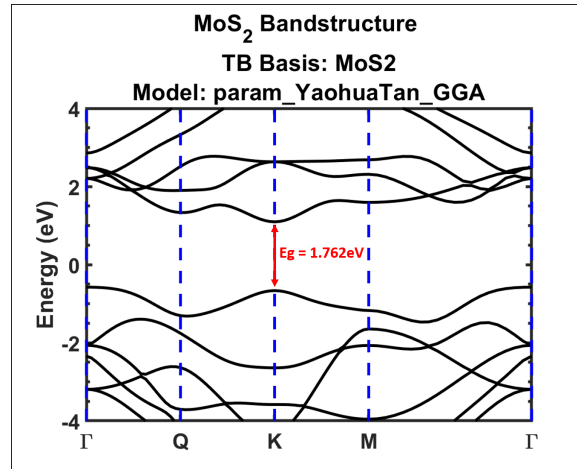
(a) NEMO simulation of monolayer MoS_2 using DFT-GGA
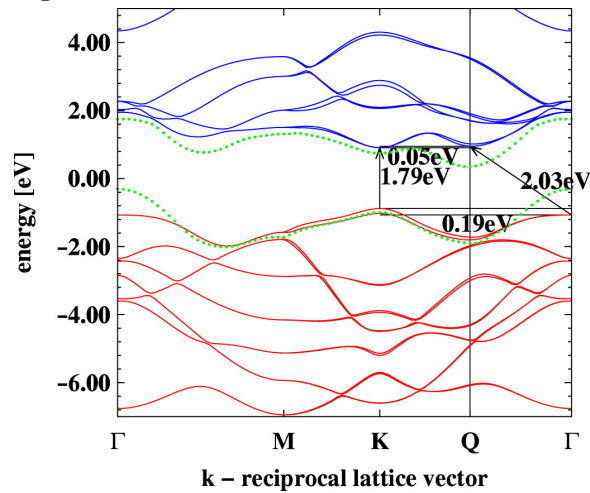
(b) E-K of single MoS_2 monolayer using VASP [19]

Figure 5.7: Simulation comparison of NEMO5 simulation of MoS_2 versus VASP [19]

boundaries. A direct band-gap of 1.76 eV was observed at K k-point in the bandstructure, which matches very closely with the band-gap of MoS_2 quoted in literature [19]. An indirect band-gap of 1.673 eV was also observed between Γ and K k-points.

Models provided in NEMO5's database factor in spin-orbit coupling as well, but not for all materials. It is a growing project at the time of working on this thesis. The presented plot is calculated without spin orbit coupling.

5.3 Tungsten Ditelluride (WTe_2)

Ab-initio simulations were conducted for WTe_2 crystal. With the space group pmn_21, both monolayer and bulk systems were simulated. Jana *et al* mentions in his work [6] how the unique magnetic properties of this material make it stand out from the other TMDs and so it is not wise to analyze this system without spin-orbit coupling. To verify this idea, we simulated the system in both the conditions, with and without spin-orbit coupling, just so it is explicitly visible how dramatic the magnetic effect is in WTe_2.

5.3.1 Crystal Structure and Band Structure

Td-WTe_2 is the most stable crystal configuration for this system. Figure 5.8 shows a visualization of WTe_2 via MedeA-VASP tool.

(a) Crystal structure bulk WTe_2, red axis="a" blue axis="b"

(b) Crystal structure monolayer WTe_2, red axis="a" blue axis="b"
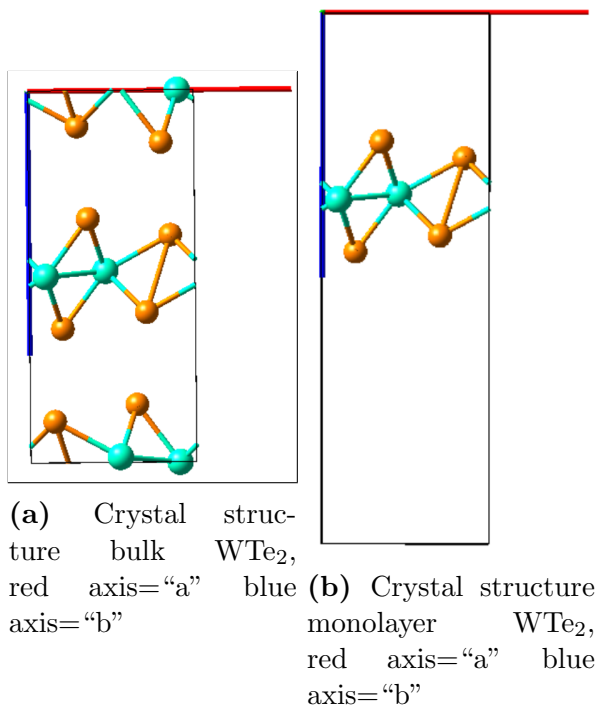
Figure 5.8: Crystal structure of WTe_2 as visualized by MedeA tool, as bulk and in monolayer

For visualizing an accurate monolayer (as the system exists in bulk by default),

following steps were taken:

- Without moving the atoms from their positions, "c" dimention (z-axis, inter-layer gap) was increased to 2 nm from 1.4 nm in order to minimize the van der Waal force of consecutive layers.

- The system's space group was dropped to p1 (primitive cell) so that the atoms could be edited independently.

- Finally, the atoms of the top and bottom layer were removed from the structure (deleted) to get the structure shown in Figure 5.8b

Using these configurations, the band structure of both bulk and monolayer systems were simulated. The Brillouin zone was sampled with 20x11x1 and 20x11x3 k-points to form the k-space matrix for monolayer and bulk systems respectively. GGA-PBE variant of the DFT functional was used to solve for the electronic properties of WTe_2 and obtain its band structure. The self-consistent algorithm (SCF) was set to converge when the difference between consecutive iterations dropped below $1e^{-5}$eV. A plane wave cut off limit of 500 eV was used. The systems were simulated with spin-orbit magnetism enabled as well as disabled.

Figure 5.9 shows $E - k$ band structure along Γ-B-S-Γ high symmetry points for both bulk and single layer. This simulation is performed without spin-orbit coupling. The plot in Figure 5.9 shows a clear overlap of valance band maxima and conduction band minima, indicating a semi-metal type characteristics. The $E - k$ plot for a single layer system, when calculated under no spin-orbit coupling, shows the same $E - k$ plot as that of the bulk system with the exception of lesser bands, i.e., this system also shows a semi-metallic property, even though experimental results and theory suggests it should be insulating [6]. Therefore, another set of simulations that included SOC (spin-orbit coupling) were performed. The results came at the expense of time and computational resources. Our simulations did not show any transition
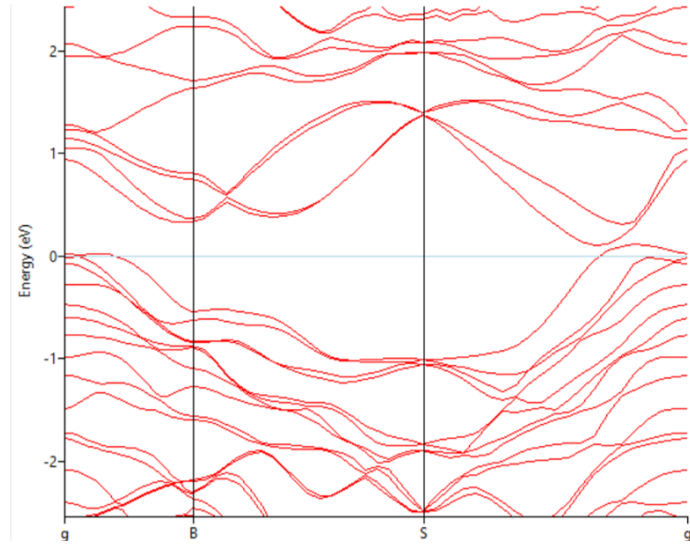
(a) Energy-k distance band structure simulated for bulk WTe_2
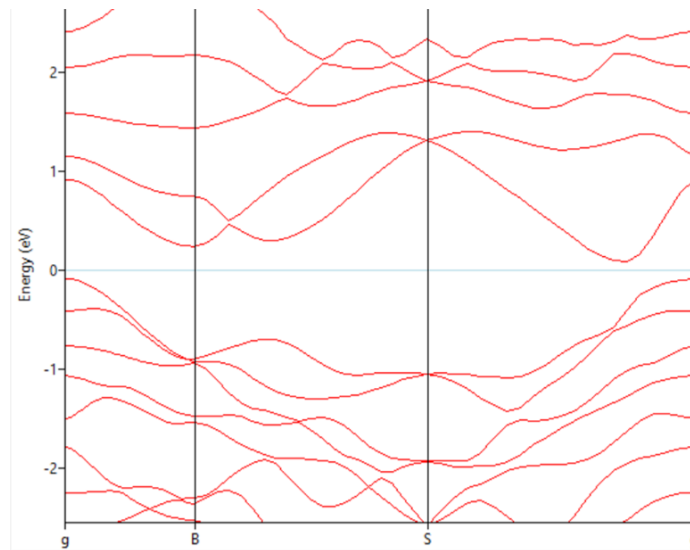
(b) Energy-k distance band structure simulated for mono-layer WTe_2

Figure 5.9: E-K band structure for WTe_2 (a) bulk system (b) monolayer system. High symmetry path = Γ-B-S-Γ. (a) semi-metal output. No band gap (b) semi-metal structure; less energy bands

to insulating behavior in the monolayer configuration. Figure 5.10 shows an overlay of band structure calculated with and without spin-orbit coupling along a different high-symmetry path than previous simulations. This band-structure follows Γ-Q-K-M high symmetry path and shows a direct band gap at **K** valley point. The plot

shows a direct band gap of 0.792 eV when calculated with spin-orbit coupling and a direct band gap of 1.2 eV when calculated without spin-orbit coupling. This shows there is a significant impact of spin orbit coupling on the electronic properties of WTe_2.

WTe$_2$ HSE06
Spin Orbit Bandstructure (solid)
No Spin Orbit (blue dashed)
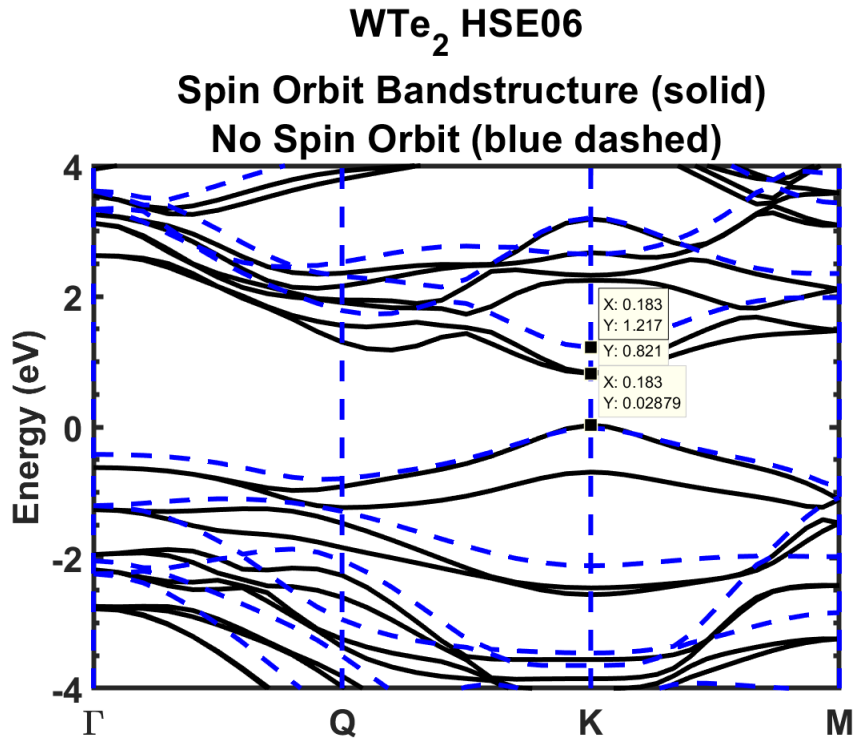
Figure 5.10: Bans-structure of monolayer WTe_2 calculated with spin orbit coupling (solid black) and without spin orbit coupling (dashed blue) using DFT-HSE06 functional in VASP

Looking at Figure 5.10, a distinct band splitting of the valence band at K-valley can be observed when the band-structure is obtained keeping spin-orbit coupling into consideration. This band splitting clearly shows how that spin-orbit coupling in calculating the electron structure for TE_2 is very crucial. Such a large difference can have a significant impact on electronic behavior like bandgap and charge mobility when the material is used in a device.

Literature like [6] and [7] quote heavy dependency of magnetic moment on tungsten ditelluride and they mention that the material is insulating in monolayer. The simulations performed in this research show that in bulk the system does show metal-

lic behavior, but in monolayer, it is semiconducting in nature with an E_g of 0.792 eV.

Now that a valid electronic band structure has been established for these three materials, they can be further used in simulating devices. In the next chapter, a tunnel field-effect transistor is simulated using monolayer of MoS_2 as a channel. NEMO5 was used to perform device simulations.

Chapter 6

<div align="right">

Device Simulations

</div>

Now that the tool has been calibrated using MoS_2, GaAs and other III-V materials and their stacks [15], this chapter discusses the simulation of an InAs Esaki diode and TFETs consisting of a monolayer channel of three TMD materials. Molybdenum disulfide, tungsten diselenide and tungsten ditelluride are used in this study as the choice of material for TFET's monolayer channel. The experiment was set up to observe the variation in I-V characteristics for different TMDs.

The flow of the chapter is as follows: The first sections describes the simulation of an InAs Esaki diode which had been fabricated and tested by David Pawlik in his research [20]. The structure of the fabricated device and its translation into a nanoTCAD equivalent structure using NEMO5 is presented to give an example of device structuring in NEMO5 input deck.

The second section discusses a TFET example with monolayer channel, its input deck structure and important parameters of the input deck. The TFET is simulated with three different TMD materials, MoS_2, WTe_2, and WSe_2. The I-V characteristics are plotted and compared for the simulated materials. This device is not compared against any literature or experimental data, as the purpose of this experiment was to understand the operation of the tool for a TFET using a material that had been previously calibrated for the tool in use, i.e., NEMO5.

6.1   InAs Esaki Diode Study

David Pawlik *et al* [20] fabricated InAs Esaki PN junction diodes using MBE (molecular beam epitaxy). They used J_p (current density) as one of the benchmarking figures. Therefore the same benchmark parameter was used in this research for the simulated structures and the obtained values were compared against the experimental results. This homojunction system was picked because of the availability of experimental results and the in-depth knowledge of its structure such that it could be confidently reproduced for the simulations. Fabricated structure had P^{++}-I-N^{++} configuration with doping densities of $1xe^{19}$ cm^{-3}, $1.6xe^{14}$ cm^{-3}, and $1.8xe^{19}$ cm^{-3} respectively. The material stack is shown in Figure 6.1.
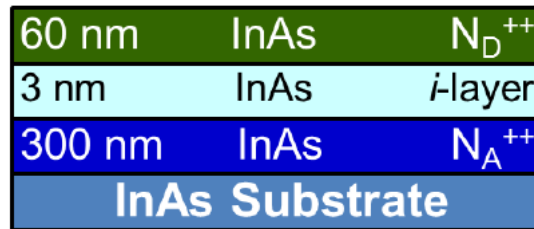
Figure 6.1: Schematic structure of InAs homojunction Esaki diode [20]

6.1.1   NEMO5 Input Deck Structure

NEMO translation of the presented system is as follows: by syntax, NEMO input deck is mainly divided into three blocks, Figure 6.2, enclosed within "curly brackets". The first block describes the **"Structure"** of the device. Within the structure block, there are **"Material blocks"**, **"Domain blocks"** and **"Geometry blocks"**. These three blocks together consist of information about the structure of the device. The correct order of structure definition is to start with the material definition. If the system contains more than one material, then different material blocks can be used with each block comprising of the material properties, the region consisting of the particular material, the priority of the material, and other necessary material characteristics.
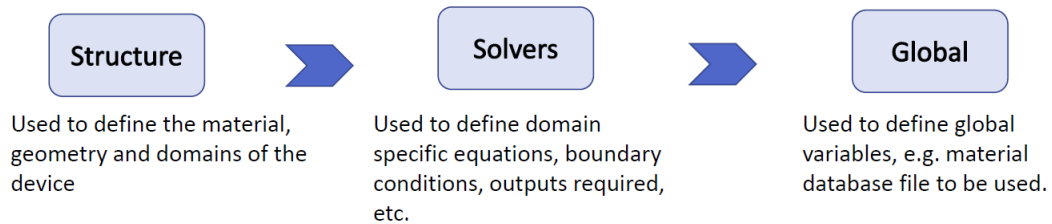
Figure 6.2: Distribution of NEMO input deck into 3 blocks

For instance, the InAs Esaki diode (PIN configuration) has three regions, P^{++}, Intrinsic and N^{++}. Therefore, one defines three material sections and uses the "region" tag to enumerate their region numbers, as shown in Figure 6.3.

```
Structure{
Material
    {
        crystal_structure = zincblende
        doping_type = N
        doping_density = 1.8E19
        name = InAs
        regions = (3)
        tag = InAs_highDoping
        /* DB Parameters */
                Bands:TB:sp3d5sstar_SO:param_set = param_HSE06_mapping

    } //Close First Material
Material
    {
        crystal_structure = zincblende
        doping_type = N
        doping_density = 1.6E14
        name = InAs
        regions = (2)
        tag = InAs_lowDoping
        /* DB Parameters */
                Bands:TB:sp3d5sstar_SO:param_set = param_HSE06_mapping

    } //Close Second Material
Material
    {
        crystal_structure = zincblende
        doping_type = P
        doping_density = 1E19
        name = AlGaSb//GaInAsSb
            x=0.4//Al
        regions = (1)
        tag = GaSb_PDoping
        /* DB Parameters */
                Bands:TB:sp3d5sstar_SO:param_set = param_HSE06_mapping

    } //Close Third Material
```

Figure 6.3: Code snippet for material definition of InAs Esaki diode

The necessary tags in the Material block are:

- Crystal structure =: defines the crystal/Brillouin zone of the material

- Doping-type and Doping-density =: N or P type doping and the doping density in cm^{-3}.

- Name =: name for that material for the code to fetch that material from their database

- Region =: Gives the region number for the defined material.

- Tag =: Identification flag for that material to be referred later in the code

- DB Parameters =: To give the name of the tight-binding parameter variable values as stored in their material database. Here it is param HSE06 mapping, which consists of fit tight binding parameters obtained and used in HSE06 functional (Hybrid functional that we discussed in theory of material characterization)

Next, one defines the domain which decides the collection of regions that make up a domain, i.e., the sections on which a similar set of numerical equations are to be solved. Device is one domain, source and drain are two others. In case of a PN junction diode, there is mp gate, but one can have the gate as another domain and so on. Each domain consists of all the regions that make up that domain: the base material for the domain (which is referred to by using the "tag" name used in material definition), overall dimensions of the domain, starting cell co-ordinates (x,y,z), name of the domain (e.g., device), periodicity of the cells (in x,y,z direction) and the leads that the domain is connected to on either end. Figure 6.4 shows a code snippet consisting domain definitions for a device and drain contact. Since QTBM and NEGF charge transport models were employed for the simulations, the device under simulation was required to have non-vanishing boundaries (semi-infinite

```
Domain
    {
        base_material = InAs_lowDoping
        crystal_direction1 = (1,0,0)
        crystal_direction2 = (0,1,0)
        crystal_direction3 = (0,0,1)
        dimension = (19,1,1)
        leads = (source_contact,drain_contact)
        name = device
        output = (xyz,coupling)
        periodic = (false,true,true)
        regions = (1,2,3)
        space_orientation_dir1 = (1,0,0)
        space_orientation_dir2 = (0,1,0)
        starting_cell_coordinate = (0,0,0)
        type = pseudomorphic
    } //Close First Domain
Domain
    {
        base_material = InAs_lowDoping
        crystal_direction1 = (1,0,0)
        crystal_direction2 = (0,1,0)
        crystal_direction3 = (0,0,1)
        dimension = (1,1,1)
        leads = (device,drain_drain_contact)
        name = drain_contact
        output = (xyz,coupling)
        periodic = (false,true,true)
        regions = (3)
        space_orientation_dir1 = (1,0,0)
        space_orientation_dir2 = (0,1,0)
        starting_cell_coordinate = (19,0,0)
        type = pseudomorphic
    } //Close Second Domain:Drain Contact
```

Figure 6.4: Code snippet of input deck showing domain definition for two domains

boundaries). To realize such a structure, the device contact leads were extended by an additional three contacts, all 1x1 unit cells.

Once the domains are defined, along with FEM domains, i.e., domains that define the aggregation of regions that need mesh refinement using FEM (finite element method), the geometry is defined using the geometry block. The final block for structure definition is the "Geometry Block". Figure 6.5 shows the description of the geometry section, which entails the geometric shape, coordinates for minimum and maximum location (x,y,z coordinates) and priority, all to be defined for each region. Generally, to avoid any band bending at the contacts, the two extreme ends of the entire geometry are extended to the edges of the domain region. The domain is the wrapper that encapsulates the geometry region. This concludes the definition of the structure of the device.

```
Geometry
    {
        Region
        {
            region_number = 1
            priority = 1
            shape = cuboid
            min = (-20,0,0) //Span to beyond domain
            max = (4.84664,2,2)
        } //End of Region (1)
        Region
        {
            region_number = 2
            priority = 1
            shape = cuboid
            min = (4.84664,0,0) //Continue from Region 1
            max = (6.66413,2,2)
        } //End of Region (2)
        Region
        {
            region_number = 3
            priority = 1
            shape = cuboid
            min = (6.66413,0,0) //Continue from Region 2
            max = (40,2,2) // Push to beyond domain
        } //End of Region (3)
    } //Close Geometry
} //Close Structure
```

Figure 6.5: Code snippet for input deck geometry section, showing the geometric description for each region, here 1,2 and 3

The "Solver Block" consists of smaller "solver" subsections, in which each solver dictates the type of simulation that needs to be performed on the given system. Each sub-section also consists of parameters and options for the task.

It should be noted that the code processing is independent of the order of parameters given in the block. This holds true for all the blocks and all the parameters. Although, the order of the blocks needs to be correct (i.e., the material block has to be defined first, and so on). Following are some of the parameters that can be included in a solver block.

- Type =: "MetaPoissonQTBM5"; name of the solver that needs to be employed for simulation.

- Name =: tag name for the solver.

- Active regions =: The regions on which this particular solver will be solved.

66

```
Solvers{
    solver
    {
        type = MetaPoissonQTBM5
        name = QTBM
        active_regions = (1,2,3)   //Device:ActiveRegion:device
        clean_all_in_reinit = true
        contact_domains = (source_contact,drain_contact)
        contact_aux = (source_source_mode_contact)
        output = (JE,NE,current,ldosn1d,ldosp1d)
        tb_basis = sp3d5sstar_SO //sp3sstar_SO//sp3d5sstar     /////// InGaAs does not
                density_of_states_output = true
        energy_grid_constructor = QTBM:adaptive_grid_generator
        number_of_MPI_ranks_in_real_space = 1 //4
        density_solver = QTBM:Transformation1
        derivative_of_density_solver = QTBM:Transformation1
        solve_on_single_replica = true
        solver_type = compression
        //Source_chemical_potential = 10
        //Drain_chemical_potential = 10
        with_poisson = true//false//true ///EDIT. Screen materials
        no_file_output = true
        debug_output_job_list = false
        regions_adjacent_to_source_electrode = 1
        regions_adjacent_to_drain_electrode = 3
        source_voltage = 0.0
        drain_voltage = 0.0
        ramper_voltage = (0,0.05,0.1,0.15,0.2,0.25,0.3,0.35,0.4,0.5,0.55,0.6,0.65,0.7)
        ramper_contact = source
        no_integration_for_transmission = true
        system_type = quasi_1D
        kxmax = 0.5
        kxmin = 0
        kymax = 0.5
        kymin = 0
        number_of_k_points = 14
        degeneracy_factor = 4
        non_rectangular_energy = true
        laplacian = (x)
```

Figure 6.6: Code snippet for input deck to simulate I-V curve for InAs Esaki diode

- tb basis =: " Tight-binding models

- ramper voltage =: list/array of voltages that sweeps the connected ramper lead/contact.

- drain and source voltages =: initial source and drain voltages

- output =: all the outputs required from the simulations, like current density (JE), drain current etc.

- residual criterion =: The convergence limit for iterations

Lastly, the global section is defined that contains the address of the material database file and the command for the list of solvers (amongst those that were defined in the solver block) that would be computed during program execution. It should be noted that one can define multiple solvers in the deck, yet command the program to run/solve only a selective few (even one). This command is given in the global block. By doing this, one can make the input deck for more than one operation and during simulations, the whole deck need not be edited in order to perform a different operation on the same device.

6.1.2 Results: InAs Esaki Diode

On simulating the similar structure in NEMO, the current density was obtained in the ball-park of the experimental value. A deviation of 17% from the experimental results was observed. The simulation failed to converge when the system entered diffusion current; the reason for this is still unknown. The hypothesis is that the contact regions were still too narrow to accommodate the equilibrium at high voltage values, along with limited computational power. But since the experiment was focused on obtaining only tunneling current, this experiment was not extended any further.

Device	N_D	NA	Experimental J$_P$	NEMO J$_P$	Error(Exp-NEMO)/Exp
InAs	$1e^{19}$	$1.8e^{19}$	37.6 kA	44 kA	17%

Table 6.1: Comparison from experimental [20] and NEMO-simulated results

The plot in Figure 6.7 shows two InAs Esaki diode's I-V, both with different doping densities. The blue plot has a 0.3:1.8 concentration ratio N_D/N_A. The peak experimental current density was found to be about 2kA [20] and showed a very clear NDR dip, but upon simulation of the same structure, peak current density of 0.575 kA per unit area was obtained, which is 71% deviated from the experimental results. Reverse-biased diffusion current is spot on with the experimental, but for the quantum
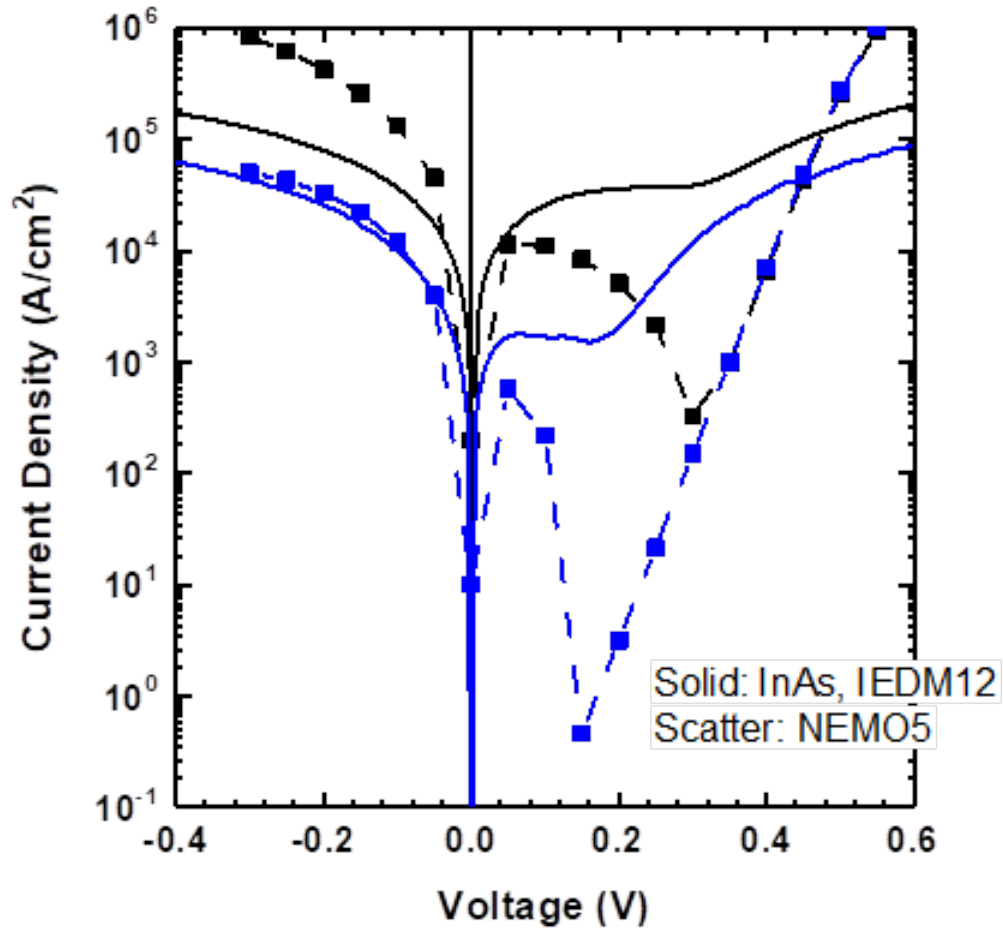
Figure 6.7: Overlay of experimental [20] and NEMO simulated I-V characteristics for InAs Esaki diode

realm, the system shows an underestimation of the current density. We argue against it on the basis of our benchmarking data, which were SIMS results obtained for the InAs substrate. The SIMS data provided us with information about the total carrier concentration, instead of the total "activated" carrier concentration. Therefore, the simulation tool considered a different concentration for activated carriers than the actual carrier densities, leading to a great difference in their output currents. The black plot, Figure 6.7, shows a similar inaccuracy. Here the simulated data is slightly overestimated in both diffusion and tunneling region. But the deviation in the tun-

neling current is within 20% of the experimental data and our primary focus was to simulate and understand the tunneling aspect of the device.

6.2   Tunnel Field-Effect Transistors: NEMO study

Another vehicle for experimenting with the characterized TMD material (MoS_2) was a tunnel field-effect transistor (TFET). This device was not studied to be compared to anything in literature or experiment. Rather it was studied to understand the operation of NEMO5 tool for a TFET using a novel material like MoS_2. This chapter deals with translating a TFET device structure into a NEMO5 input deck and simulating the system to obtain I-V characteristics of the device. A VTK file for the visualization of the obtained structure is also presented.

6.2.1   Device Structure in simulation

The same block flow as that of Esaki diode is followed for TFET device description. The additional regions and more domains get defined for a TFET in comparison to a tunnel diode. MoS_2 TFET was simulated using QTBM numerical methods with material fitted from the tight binding parameters obtained from DFT-GGA. MoS_2 lattice constant "a" was set to be 0.316 nm. The conduction band edge was set to be at 1.1 eV and the valence band edge was set to be at -0.58 eV. Doping densities of source, intrinsic body and drain were set to be $1e^{20}$ cm^{-3} (P++ type), $1e^{14}$ cm^{-3} (N type) and $1e^{20}$ cm^{-3} (N++ type), respectively. A layer of oxide was set up as the top gate dielectric, with a dielectric constant of 24. After the material set up, the domain for the device was set up. The total length and height of the device (gate+oxide thickness) were set to be 64 unit cells in length, 1 unit cell in width and 5 unit cells in height. The source contacts and its auxiliary source contacts were connected to the left extending to 20 unit cells and drain contacts to the right extending up-to 70 unit cells to the right of the device. The structure is given in Figure 6.8.
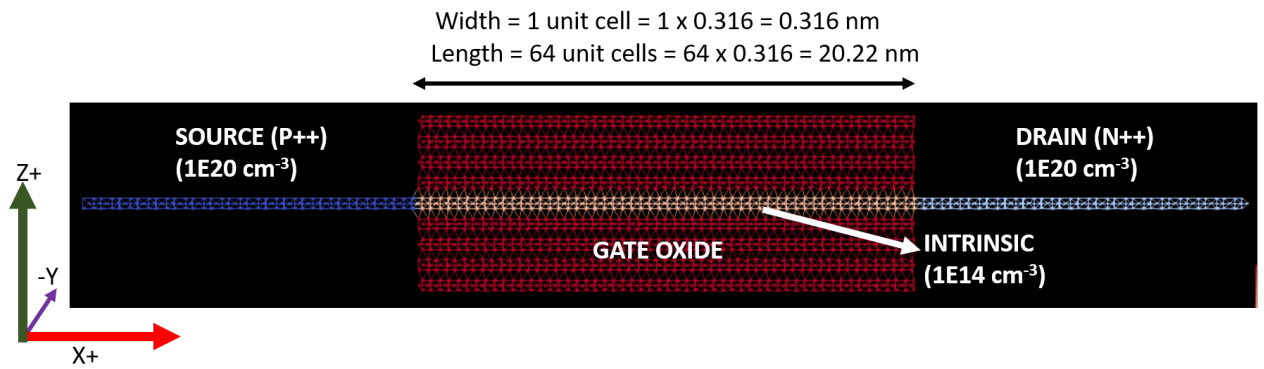
Figure 6.8: Visualization of MoS_2 channel based TFET with 4 regions, source, drain, intrinsic and gate, using NEMO5. Width of the device is in the y-axis direction; length of the device is along x-axis
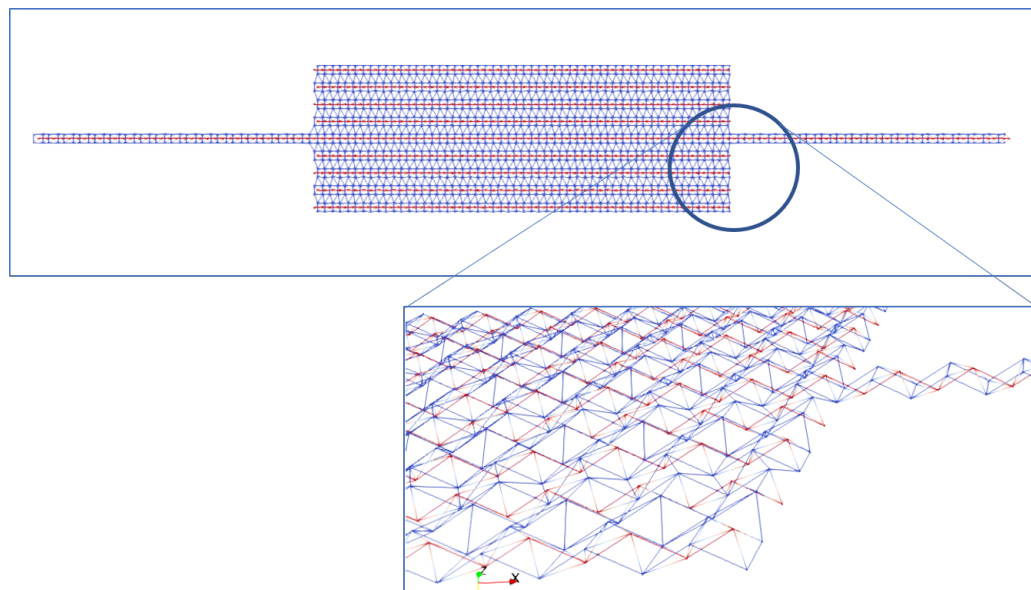
Figure 6.9: Visualization of the described device with a close-up image of its surface using NEMO5. The surface image shows in a wireframe representation the atomic mesh arrangement.

Figure 6.9 shows a wireframe representation of the structure, wherein the middle cuboid is the device region, extending to 64 unit cells, and two thin (single unit cell thick) source and drain extensions are a combination of all the auxiliary source and drain connections, defined to give a semi-infinite boundary to the system.

While defining the solvers, QTBM was used as the charge transport solver, that self-consistently iterates between the Poisson equation and Schrodinger's equation

|	MoS$_2$	WTe$_2$	WSe$_2$
ϵ_a (dielectric)	4.2	5.7	4.5
ϵ_c (dielectric)	2.8	3.3	2.9
BandEdge Ev (eV)	-0.58	1.9	0.4
BandEdge Ec (eV)	1.1	2.6	1.8
TB parameter set	GGA (no SOC)	GGA (SOC)	GGA (no SOC)

Table 6.2: Table containing material properties set up in MoS$_2$, WTe$_2$, and WSe$_2$ TFETs

until the value converges. The limit for convergence is set to be $1e^{-3}$ with initial value set at 2.5 V. This value was selected on heuristic basis factoring in the speed of convergence. It was observed that few voltage points took more iterations and longer duration to converge than others. Using the same device specifications as MoS$_2$ TFET two more TFETs were simulated; one with a monolayer channel of WSe$_2$ and another with a monolayer channel of WTe$_2$. Table 6.2 presents the material parameters set up for the three FET devices. In the table ϵ_a and ϵ_c refer to the dielectric constant of the channel material in the given lattice direction. This parameter determines the conductivity of the channel material in a particular direction. Therefore, by aligning the material in such a way that offers high conductivity in the direction of current and low conductivity in the direction perpendicular to the flow of current can help in reduction of gate leakage current.

6.2.2   Device Characteristics: I-V Curve Analysis

On applying a potential to the gate, the energy bands of the channel bend such that the conduction band edge of the channel region overlaps with the valence band edge of the source region. The gate voltage at which such a band configuration is attained and which leads to the onset of tunneling current is the threshold voltage for a TFET. Figure 6.10 shows the band bending of the source, channel, and drain region for the WSe$_2$ TFET simulated using NEMO5. The system is operated at a drain voltage of 0.5 V.

The left figure shows the device band structure when the device is in off state, at a
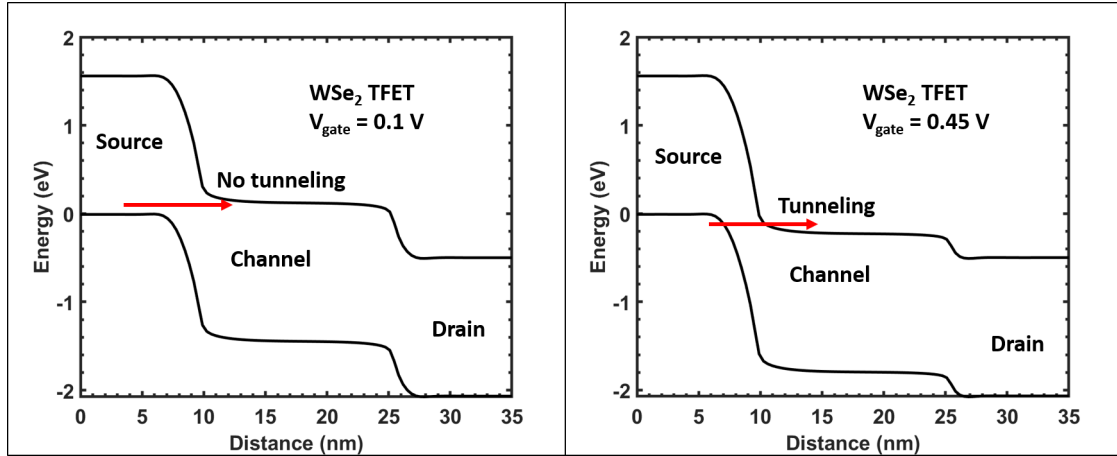
Figure 6.10: Source-channel-drain energy band bending for WSe$_2$ TFET. V$_G$ = 0.1 V (Left) showing off state of TFET and V$_G$ = 0.45 V (Right) showing ON state of the TFET. V$_D$ is set at 0.5 V.

gate voltage of 0.1 V. The figure shows no overlap between the conduction band edge of the channel and valence band edge of the source, therefore, no tunneling window is present in the device, rendering the device operation off.

Due to the absence of an inverted channel at the surface in a TFET along with completely depleted body/substrate, the off current in a TFET cannot be defined by the carrier concentration at the surface, like in a MOSFET. Therefore, for a TFET a reasonably small drain current is accepted as off current. The value of off current is accepted to be 1nA/ μm.

Corresponding to V$_G$ of 0.1 V, Figure 6.11 shows the output current for the WSe$_2$ system (black plot). Figure 6.11 shows the drain current to be less than 1 nA/μm ($\approx$ 10^{-9} nA/μm) for WSe$_2$ at gate voltage of 0.1 V, therefore the device is considered off at V$_G$ equal to 0.1 V.

At a gate voltage of 0.45 V, right side figure of Figure 6.10 shows a clear overlapping of E$_C$ of the channel with E$_V$ of the source, therefore allowing electrons to tunnel through from source to channel leading to significant drain current. A corresponding drain current of 1 μA/μm for WSe$_2$ TFET can be seen in Figure 6.11 (black plot). Such high drain current clearly indicates the device to be in ON state.
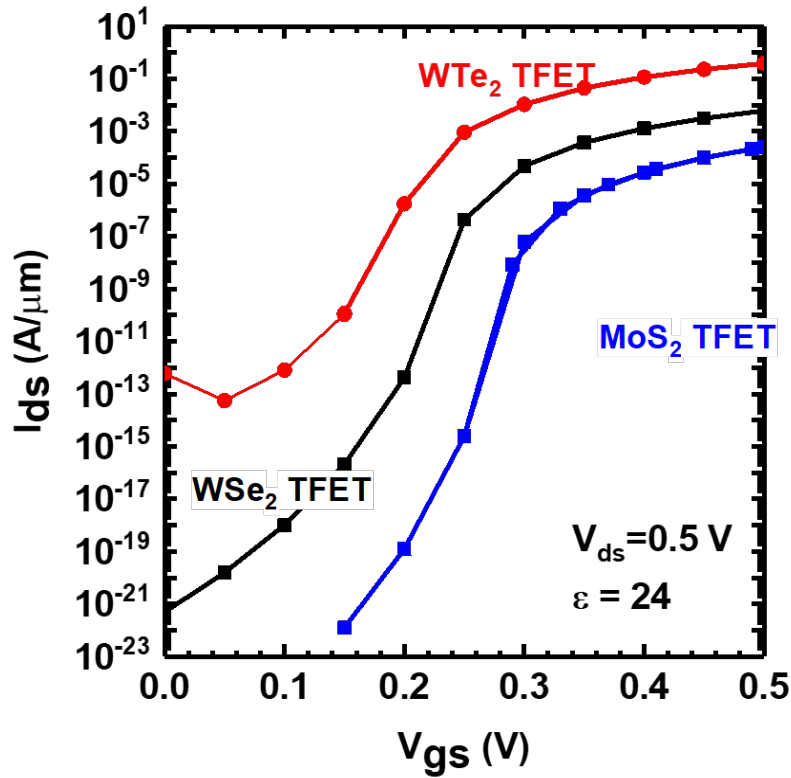
Figure 6.11: I-V curves for MoS_2, WSe_2, and WTe_2 TFETs with $V_D = 0.5$ V and gate dielectric constant $= 24$.

Figure 6.11 also includes the I-V characteristics obtained for MoS_2 TFET and WTe_2 TFET. WTe_2 TFET gate voltage was swept from 0.05 V to 1 V and MoS_2 TFET gate voltage was swept from 0.15 V to 0.89 V. Upon simulating the three TFETs, device parameters shown in Table 6.3 were obtained. The results show that WTe_2 can produce the highest drain current but has the largest subthreshold swing in comparison to WSe_2 and MoS_2. The Figure 6.11 and Table 6.3 shows that WSe_2 as the channel material for a TFET can produce an optimal device operation with small enough sub-threshold swing and good drive current of over 1 μA / μm.

Among the three materials simulated, WTe_2 is known to show significant magnetic properties due to strong spin-orbit coupling. The simulation of WTe_2 TFET, when operated under a high drain voltage of 0.5 V, showed a significant drain current flow

	$\mathbf{MoS_2}$	$\mathbf{WSe_2}$	$\mathbf{WTe_2}$
SS (mV/dec)	9.09	13.63	16.67
V_{th} (V)	0.3	0.25	0.25
V_{off} (V)	0.2	0.15	0.1
I_{peak} (A/μm)	10^{-4}	$2\mathrm{x}10^{-3}$	$2\mathrm{x}10^{-1}$
I_{off} (A/μm)	10^{-19}	10^{-16}	10^{-12}

Table 6.3: Tabulating device characteristics for three TFETs. $V_D = 0.5$ V. Gate dielectric constant $= 24$. Channel length $= 20$ nm. (The sub-threshold swing is calculated from the curves. The values are not compared against practical devices)

as well as when the device was operated at a gate voltage of 0.35 V. Figure 6.13 shows the I-V characteristics of WTe$_2$ TFET simulated at two different drain voltages; 0.1 V and 0.5 V. Band diagrams shown in Figure 6.12 shows the tunneling window opening at both 0.35 V gate voltage (Fig 6.12 (c)) and at a gate voltage of -0.2 V (Fig 6.12 (a)). At V_G of -0.2 V, the conduction band edge of the drain overlaps with the valence band edge of the channel region, thereby allowing tunneling current to flow from channel to drain. At V_G of 0.35 V, the conduction band edge of the channel overlaps the valence band edge of the source, thereby allowing tunneling current to flow from source to channel.

At low drain voltage of 0.1 V, the device shows normal non-ambipolar behavior, that is, turns off at low biasing of gate voltage. (Figure 6.13)
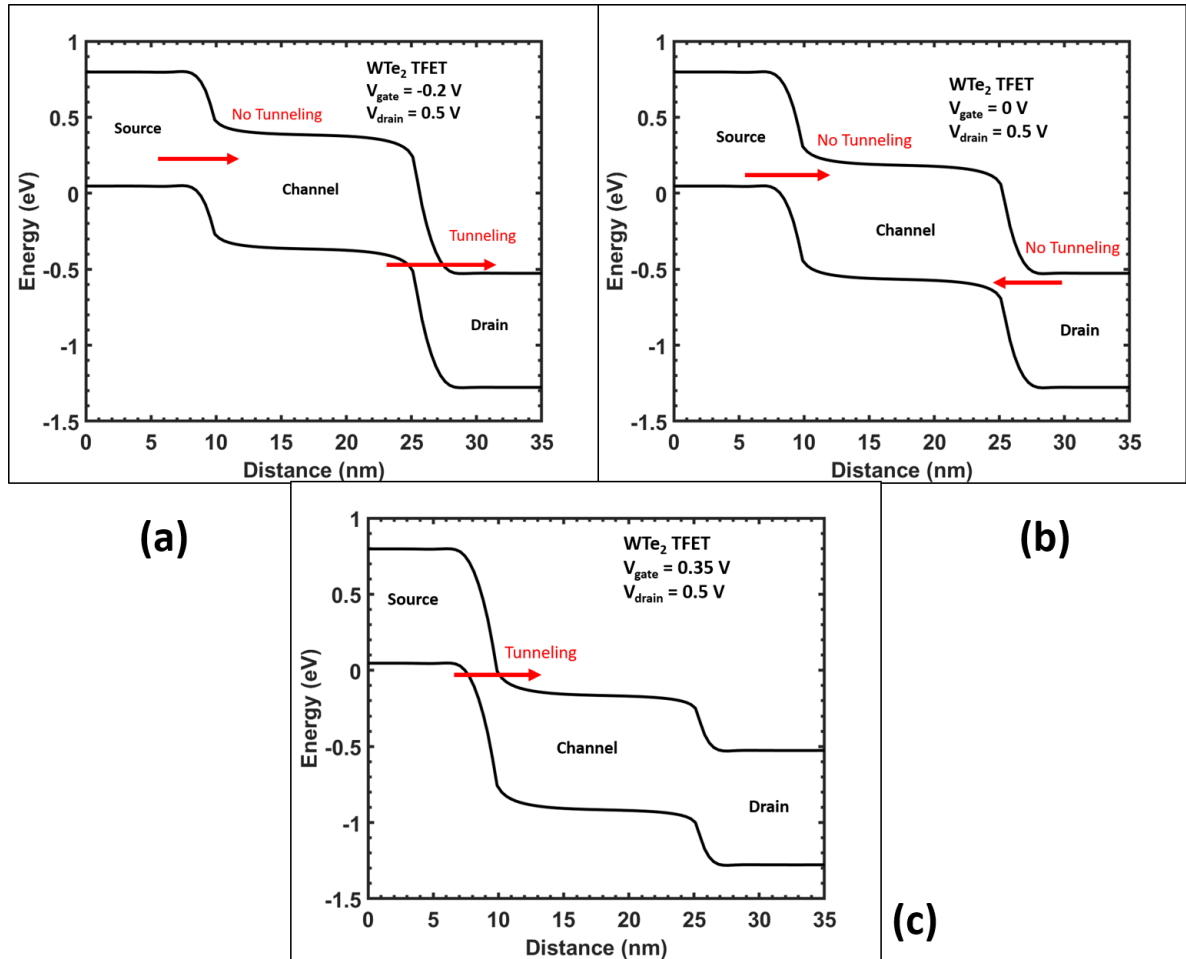
Figure 6.12: Band diagram for WTe$_2$ TFET at V$_D$ = 0.5 V and V$_G$ = -0.2 V, 0 V and 0.35 V. The band diagram shows off state at 0V and tunneling state at both -0.2 V and 0.35 V. Figure shows ambipolarity in WTe$_2$ TFET.
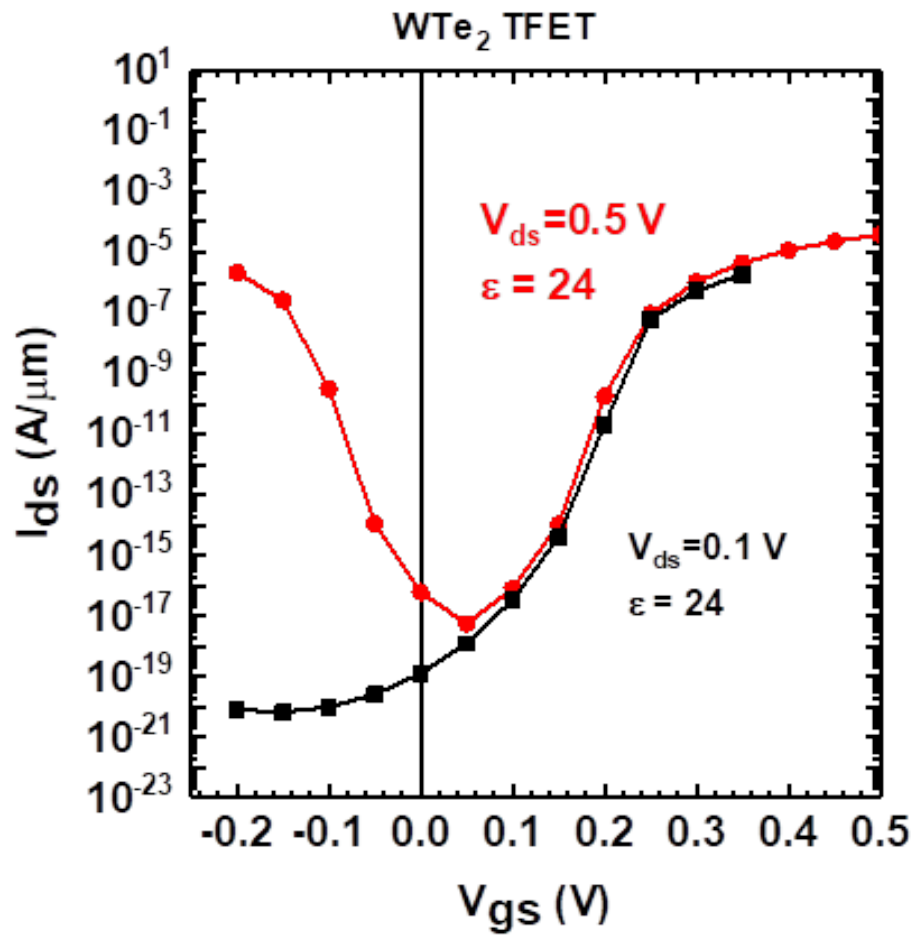
Figure 6.13: I-V characteristics for WTe$_2$ TFET under two different drain voltages: 0.1 V and 0.5 V. Figure shows ambipolarity in WTe$_2$ TFETs at higher drain voltage

Chapter 7

Conclusion and future work

This project was meant to be an initiation in the realm of atomistic simulation. Through this work, we intended to explore the operational mechanics of atomistic tools like VASP and NEMO5. For the first time at RIT, an atomistic approach was taken to understand and simulate material band gaps and tunneling devices. The approach towards a simulation-based study was chosen to restrict the fabrication tests to only those scenarios that cannot be successfully modeled and simulated as of now. The project looked into the calibration process of NEMO5 and VASP, first using a known material like GaAs and then novel materials like TMDs. It is clear that there is a gap between experimental and simulated values but we were able to calibrate the tool for MoS_2 within an error margin of 10%. The validity of these results still depends on further experiments that need to be conducted in order to get a consensus on the information. We understood the effect of spin-orbit coupling in materials and how the inclusion of SOC brings the results closer to reality, although at the expense of time and computational power. The operation of an atomistic tool NEMO5 was self-taught using the top-down approach which led to an increased understanding of how the numerical models get interpreted by code. The highlight of this project was a new point of view regarding device modeling and a method of learning was developed which would in the future prove immensely helpful in interpreting and understanding the dynamically changing technology. Using MoS_2 as a pivot, the

tool was benchmarked for bandgap and using silicon, the tool was benchmarked for computational time. Finally, as an exercise to test our understanding of atomistic devices, InAs tunnel diode and MoS_2 monolayer-based TFET was simulated and I-V characteristics were obtained. This study concluded with enough understanding of atomistic modeling that further learning can be self-driven.

This work was instrumental in showing the need for a lot of work in atomistic simulation region. There is a need for more experimental material data to be able to generate effective models and then further research is needed understanding the computational efficiency and power need of the numerical models used for quantum computations. Further research in strain analysis and spin-orbit band splitting is needed to push the simulations closer to realistic values. This would ensure better tunneling and quantum device design and fabrication. More input is needed in understanding the magnetic properties of materials like WS_2 and WTe_2 to be able to utilize their properties. Another immediate extension to this work can be in simulating other materials like WS_2 and WSe_2 and validating the system's calibrations against the MoS_2 calibration. There is a need to understand the NEMO parameters and its material data file to speed up the simulation and obtain controlled results. Very little work was done in this project regarding the scattering model, Recursive Green's Function (RGF) or NEGF and therefore this project was limited to materials that did not show scattering effects. This was also because this study was based primarily on mono-layers, wherein no scattering is observed. But in experiments with materials like silicon, a better understanding of the scattering models is required.

Furthermore, tampering with the bowing parameters, strain parameters, band edges and lattice constants in the material file can give great insight into the workings of the material. A better understanding of the effect of Brillouin zone high symmetry point paths is important to design the material stacks. Knowing how many materials have different properties in different orientations, information about the high density

of states in the direction of transport and low density in the transverse direction can lead to effective device architecture even from material point of view. But, first and foremost, there needs to be better and efficient awareness of the need for more simulation-based studies.

References

[1] W. Choi, N. Choudhary, G. H. Han, J. Park, D. Akinwande, and Y. H. Lee, "Recent development of two-dimensional transition metal dichalcogenides and their applications," *Materials Today*, vol. 20, no. 3, pp. 116 – 130, 2017. [Online]. Available: http://www.sciencedirect.com/science/article/pii/S1369702116302917

[2] M. Pumera and A. H. Loo, "Layered Transition-Metal Dichalcogenides (MoS2 and WS2) for Sensing and Biosensing," *TrAC Trends in Analytical Chemistry*, vol. 61, pp. 49 – 53, 2014. [Online]. Available: http://www.sciencedirect.com/science/article/pii/S0165993614001344

[3] A. V. Kolobov and J. Tominaga, *Two-Dimensional Transition-Metal Dichalco-genides.* Springer Series in Materials Science, 2016, vol. 239.

[4] J. Kopaczek, M. P. Polak, P. Scharoch, K. Wu, B. Chen, S. Tongay, and R. Kudrawiec, "Direct Optical Transitions at K- and H-point of Brillouin Zone in Bulk MoS2, MoSe2, WS2, and WSe2," *Journal of Applied Physics*, vol. 119, no. 23, p. 235705, 2016. [Online]. Available: https://doi.org/10.1063/1.4954157

[5] J. Gao, D. Nandi, and M. Gupta, "Density Functional Theory Projected Local Density of States Based Estimation of Schottky Barrier for Monolayer MoS2," *Journal of Applied Physics*, vol. 124, no. 1, p. 014502, 2018.

[6] M. K. Jana, A. Singh, D. J. Late, C. R. Rajamathi, K. Biswas, C. Felser, U. V. Waghmare, and C. N. R. Rao, "A Combined Experimental and Theoretical Study of the Structural, Electronic and Vibrational Properties of Bulk and Few-Layer Td-WTe2," *Journal of Physics-Condensed Matter*, vol. 27, no. 28, Jul 22 2015.

REFERENCES

[7] W. Tian, W. Yu, X. Liu, Y. Wang, and J. Shi, "A Review of the Characteristics, Synthesis, and Thermodynamics of Type-II Weyl Semimetal WTe2," *Materials*, vol. 11, no. 7, 2018. [Online]. Available: http://www.mdpi.com/1996-1944/11/7/1185

[8] A. Klein, S. Tiefenbacher, V. Eyert, C. Pettenkofer, and W. Jaegermann, "Electronic Band Structure of Single-Crystal and Single-Layer WS_2 : Influence of Inter Layer Van Der Waals Interactions," *Phys. Rev. B*, vol. 64, p. 205416, Nov 2001. [Online]. Available: https://link.aps.org/doi/10.1103/PhysRevB.64.205416

[9] [Online]. Available: http://what-when-how.com/electronic-properties-of-materials/semiconductors-electrical-properties-of-materials-part-4

[10] B. Romanczyk, P. Thomas, D. Pawlik, S. L. Rommel, W.-Y. Loh, M. H. Wong, K. Majumdar, W.-E. Wang, and P. D. Kirsch, "Benchmarking Current Density in Staggered Gap In0.53Ga0.47As/GaAs0.5Sb0.5 Heterojunction Esaki Tunnel Diodes," *Applied Physics Letters*, vol. 102, no. 21, p. 213504, 2013. [Online]. Available: https://doi.org/10.1063/1.4808362

[11] J. Luo, J. Chen, Q. Wu, Z. Chai, J. Zhou, T. Yu, Y.-J. Dong, L. Li, W. Liu, C. Qiu, and x. Wang, "A Tunnel Diode Body Contact Structure for High-Performance SOI MOSFETs," *IEEE Transactions on Electron Devices*, vol. 59, pp. 101–107, 01 2012.

[12] A. M. Ionescu and H. Riel, "Tunnel Field-Effect Transistors as Energy-Efficient Electronic Switches," *Nature*, vol. 479, November 2011.

[13] E. G. Marin, M. Perucchini, D. Marian, G. Iannaccone, and G. Fiori, "Modeling of Electron Devices Based on 2-D Materials," *IEEE Transactions on Electron Devices*, vol. 65, no. 10, pp. 4167–4179, Oct 2018.

[14] "Jacob's ladder of density functional approximations for the exchange-correlation energy," in *AIP Conference Proceedings*, vol. 577, 2001.

[15] P. Cadareanu, "A quantum simulation study of iii-v esaki diodes and 2d tunneling field-effect transistors," Master's thesis, Rochester Institute of Technology, 2018.

[16] G. Klimeck, S. Agarwal, and Z. Jiang, "Nanoelectronic Modeling Lecture 20: NEGF in a Quasi-1D Formulation," Jan 2010. [Online]. Available: https://nanohub.org/resources/8203

[17] E. Polizzi and S. Datta, "Multidimensional Nanoscale Device Modeling: The Finite Element Method Applied to the Non-Equilibrium Green's Function Formalism," in *2003 Third IEEE Conference on Nanotechnology, 2003. IEEE-NANO 2003.*, Aug 2003, pp. 40–43 vol.2.

[18] I. G. Buda, C. Lane, B. Barbiellini, A. Ruzsinszky, J. Sun, and A. Bansil, "Characterization of thin film materials using scan meta-gga, an accurate nonempirical density functional," *Scientific Reports*, vol. 7, pp. 44 766 EP –, Mar 2017, article. [Online]. Available: https://doi.org/10.1038/srep44766

[19] E. S. Kadantsev and P. Hawrylak, "Electronic Structure of a Single MoS2 Monolayer," *Solid State Communications*, vol. 152, no. 10, pp. 909 – 913, 2012.

[20] D. Pawlik, B. Romanczyk, P. Thomas, S. Rommel, M. Edirisooriya, R. Contreras-Guerrero, R. Droopad, W. . Loh, M. H. Wong, K. Majumdar, W. . Wang, P. D. Kirsch, and R. Jammy, "Benchmarking and Improving III-V Esaki Diode Performance With a Record 2.2 MA/cm2 Peak Current Density to Enhance TFET Drive Current," in *2012 International Electron Devices Meeting.* IEEE, 2012, pp. 27.1.1–27.1.3.

[21] "International Technology Roadmap for Semiconductor," Tech. Rep. [Online]. Available: http://www.itrs2.net

[22] E. Pop, R. Dutton, and K. Goodson, "Thermal analysis of ultra-thin body device scaling [soi and finfet devices]," in *IEEE International Electron Devices Meeting 2003*, Dec 2003, pp. 36.6.1–36.6.4.

[23] S. Salahuddin, K. Ni, and S. Datta, "The Era of Hyper-Scaling in Electronics," *Nature Electronics*, vol. 1, 2018.

[24] J. E. Fonseca, T. Kubis, M. Povolotskyi, B. Novakovic, A. Ajoy, G. Hegde, H. Ilatikhameneh, Z. Jiang, P. Sengupta, Y. Tan, and G. Klimeck, "Efficient and Realistic Device Modeling from Atomic Detail to the Nanoscale," *Journal of Computational Electronics*, vol. 12, no. 4, pp. 592–600, 2013.

[25] O. M. Van 't Erve, A. T. Hanbicki, A. L. Friedman, K. M. McCreary, E. Cobas, C. H. Li, J. T. Robinson, and B. T. Jonker, "Graphene and Monolayer Transition-Metal Dichalcogenides: Properties and Devices," *Journal of Materials Research*, vol. 31, no. 7, p. 845877, 2016.

[26] F. A. Rasmussen and K. S. Thygesen, "Computational 2D Materials Database: Electronic Structure of Transition-Metal Dichalcogenides and Oxides," *The Journal of Physical Chemistry C*, vol. 119, no. 23, pp. 13 169–13 183, 2015. [Online]. Available: https://doi.org/10.1021/acs.jpcc.5b02950

[27] A. Szab, C. Klinkert, D. Campi, C. Stieger, N. Marzari, and M. Luisier, "Ab Initio Simulation of Band-to-Band Tunneling FETs With Single- and Few-Layer 2-D Materials as Channels," *IEEE Transactions on Electron Devices*, vol. 65, no. 10, pp. 4180–4187, Oct 2018.

[28] "How much is the quantum computing market worth?" Tech. Rep., September 2018. [Online]. Available: https://seekingalpha.com/article/4208355-much-quantum-computing-market-worth

REFERENCES

[29] C. Gong, H. Zhang, W. Wang, L. Colombo, R. M. Wallace, and K. Cho, "Band Alignment of Two-dimensional Transition Metal Dichalcogenides:Application in Tunnel Field Effect Transistors," *Applied Physics Letters*, vol. 107, 2015.

[30] H. Ilatikhameneh, Y. Tan, B. Novakovic, G. Klimeck, R. Rahman, and J. Appenzeller, "Tunnel Field-Effect Transistors in 2-D Transition Metal Dichalcogenide Materials," *IEEE Journal on Exploratory Solid-State Computational Devices and Circuits*, vol. 1, pp. 12–18, Dec 2015.

[31] X. Li and H. Zhu, "Two-Dimensional MoS2: Properties, Preparation, and Applications," *Journal of Materiomics*, vol. 1, no. 1, pp. 33 – 44, 2015. [Online]. Available: http://www.sciencedirect.com/science/article/pii/S2352847815000040

[32] S. G. Sorensen, H. G. Fuchtbauer, A. K. Tuxen, A. S. Walton, and J. V. Lauritsen, "Structure and Electronic Properties of In-Situ Synthesized Single-Layer MoS2 on a Gold Surface," *ACS Nano*, vol. 8, no. 7, pp. 6788–6796, 2014, pMID: 24938884.

[33] K. Dolui, I. Rungger, D. Pemmaraju, and S. Sanvito, "Possible Doping Strategies for MoS2 Monolayers: An ab initio Study," *Physical Review B*, vol. 88, 08 2013.

[34] E. Bucher, *Photoelectrochemistry and Photovoltaics of Layered Semiconductors*, A. Aruchamy, Ed. Springer Netherlands, 1992, vol. 14.

[35] J. Gusakova, X. Wang, L. L. Shiau, A. Krivosheeva, V. Shaposhnikov, V. Borisenko, V. Gusakov, and B. K. Tay, "Electronic Properties of Bulk and Monolayer TMDs: Theoretical Study Within DFT Framework (GVJ-2e Method)," *physica status solidi (a)*, vol. 214, no. 12, p. 1700218, 2017. [Online]. Available: https://onlinelibrary.wiley.com/doi/abs/10.1002/pssa.201700218

[36] Wikipedia contributors, "Transmission coefficient — Wikipedia, the free encyclopedia," 2018, [Online; accessed 15-December-2018]. [Online]. Available: https://en.wikipedia.org/w/index.php?title=Transmission_coefficient&oldid=868295621

[37] L. Esaki, "Discovery of the tunnel diode," *IEEE Transactions on Electron Devices*, vol. ED-23, no. 7, pp. 644–647, July 1976.

[38] S. M. Sze, *The Physics of Semiconductor Devices*, 3rd ed. A John Wiley & Sons, Inc., 2007.

[39] P. Hohenberg and W. Kohn, "Inhomogeneous Electron Gas," *Phys. Rev.*, vol. 136, pp. B864–B871, Nov 1964. [Online]. Available: https://link.aps.org/doi/10.1103/PhysRev.136.B864

[40] W. Kohn and L. J. Sham, "Self-Consistent Equations Including Exchange and Correlation Effects," *Phys. Rev.*, vol. 140, pp. A1133–A1138, Nov 1965. [Online]. Available: https://link.aps.org/doi/10.1103/PhysRev.140.A1133

[41] K. Berland, V. R. Cooper, K. Lee, E. Schrder, T. Thonhauser, P. Hyldgaard, and B. I. Lundqvist, "Van Der Waals Forces in Density Functional Theory: A Review of the VdW-DF Method," *Reports on Progress in Physics*, vol. 78, no. 6, p. 066501, 2015. [Online]. Available: http://stacks.iop.org/0034-4885/78/i=6/a=066501

[42] C. S. Lent and D. J. Kirkner, "The Quantum Transmitting Boundary Method," *Journal of Applied Physics*, vol. 67, no. 10, pp. 6353–6359, 1990.

[43] Y. He, T. Kubis, M. Povolotskyi, J. Fonseca, and G. Klimeck, "Quantum transport in nemo5: Algorithm improvements and high performance implementation," 09 2014.

[44] M. Paulsson, "Non Equilibrium Green's Functions for Dummies: Introduction to the One Particle NEGF equations," *arXiv e-prints*, pp. cond–mat/0 210 519, Oct. 2002.